Journal of Computational Physics 540 (2025) 114293

Contents lists available at ScienceDirect

Journal of Computational Physics

journal homepage: www.elsevier.com/locate/jcp

An interpolated bounce-back based lattice Boltzmann method for floating structures interacting with free surface flows

Baoming Guo [a], Jianping Meng [b], Dezhi Ning [c], Zhihua Xie [a,*], Shunqi Pan [a,*]

[a] Hydro-environmental Research Centre, School of Engineering, Cardiff University, CF24 3AA UK
[b] Research IT, IT Services, University of Liverpool, L69 3GG UK
[c] State Key Laboratory of Coastal and Offshore Engineering, Dalian University of Technology, Dalian 116024, China

ARTICLE INFO

Keywords:
Floating structures
Fluid-structure interaction (FSI)
Free surface flows
Galilean-invariant momentum exchange method (GIMEM)
Volume-of-fluid (VOF) method
lattice Boltzmann method (LBM)

ABSTRACT

Within the lattice Boltzmann method (LBM), we develop a new numerical model for accurately and robustly simulating the coupled interaction between air-water flows and partially submerged floating rigid bodies. The computational approach integrates the interpolated bounce-back fluid-structure interaction (FSI) method with a volume-of-fluid (VOF) approach for simulating two-phase immiscible fluid flows. We introduce the consistent initial condition iteration as the refilling scheme for new-born fluid nodes and implement a dynamic-pressure framework in the present numerical model, both for mitigating severe force fluctuations caused by the staircase geometric approximation and force imbalance between hydrostatic pressure gradient and gravity. To accurately evaluate hydrodynamic forces acted on floating bodies, which depend on submerged depth, a hydrostatic pressure-related molecular equilibrium distribution function implemented in a sub-grid system is incorporated into the Galilean-invariant momentum exchange method (GIMEM). Moreover, a set of gas-liquid-solid interface identification rules is proposed to suppress spurious currents that cause unphysical liquid adhesion to the solid surface. The developed LBM model is validated through six benchmark cases in both hydrostatic and dynamic scenarios, systematically progressing from fully submerged to partially submerged structures and from stationary to moving configurations: a free-settling immersed circular particle, static buoyant circular cylinder, water exit of a circular cylinder with prescribed velocities, dam-break flow over an obstacle, and water enter of a circular cylinder, and water wave interaction with a free-floating rectangular box. The numerical results compared to available experiments demonstrate the model's accuracy and robustness in predicting nonlinear free surface deformations and the motion responses of partially submerged structures interacting with air-water flows.

1. Introduction

Partially submerged structures interacting with free surface flows are extensively related to various research topics in ocean and coastal engineering, such as evaluating slamming forces on ship hulls or landing seaplanes [1], extracting power from offshore wave energy converters [2,3], and assessing the coastal protection provided by 'bio-shields' like mangroves [4]. For efficient numerical fluid simulations on parallel computing architectures, the lattice Boltzmann method (LBM) has developed as a promising alternative to

* Corresponding authors.
E-mail addresses: zxie@cardiff.ac.uk (Z. Xie), pans2@cardiff.ac.uk (S. Pan).

https://doi.org/10.1016/j.jcp.2025.114293
Received 17 March 2025; Received in revised form 7 August 2025; Accepted 10 August 2025
Available online 11 August 2025

classical discrete Navier-Stokes equation (NSE)-based approaches for computational fluid dynamics (CFD). Since each computational lattice in LBM updates its hydrodynamic quantities independently, it indicates no requirement of special treatment to complex boundaries and enables massive parallelization without complex data dependencies [5]. Like pseudo compressible methods, the LBM does not involve the Poisson pressure equation to impose the fluid incompressibility constraint [6,7]. Despite sacrificing exact geometric incompressibility, the computational efficiency of LBM has been considerably enhanced for numerical fluid simulations [8]. In recent years, LBM has been extensively developed for modeling free surface flows and immersed structure-fluid interactions [9–13]. However, its application to partially submerged or floating structures, as those aforementioned cases [1–4], remains challenging due to complex coupling treatments between interface capturing and fluid-structure interaction techniques.

Within the LBM, various approaches for single-phase FSI have been proposed for immersed structures-fluid interactions, without involving free surface flows [7]. These approaches typically consist of three imperative aspects in the treatment of the fluid-solid interface: 1) reconstructing the unknown distribution functions (DFs), adhering to the no-slip boundary conditions at the moving fluid-solid interface; 2) determining the motion of rigid bodies which requires accurate calculation of the hydrodynamic forces; and 3) refilling scheme, i.e., constructing the distribution functions for the fresh nodes that are converted from previous solid nodes as structures move relative to the fixed Eulerian fluid grids. Boundary conditions (BCs) are broadly classified into direct and indirect methods, based on the common hybrid framework of the Eulerian description for fluid and Lagrangian description for solid. Classically, a bounce-back (BB) scheme originally proposed by Ladd [14] is the most popular and extensively-used direct approach in LBM simulations due to its straightforward implementation and intuitive kinematic principle. However, the original BB scheme demonstrates limitations in accuracy as it employs a simplest cut-cell meshing technique, namely the staircase approximation, compared to other more accurate piecewise linear cut-cell approaches [15]. Various interpolation method have been proposed to improve the numerical accuracy on complex curved geometries, e.g., Mei's scheme [16], Yu's double interpolation [17], and Ginzburg's multi-reflection [12]. On the other hand, indirect approaches use an equivalent force to recover the fluid-solid interface with the desired properties. Most of indirect methods applied in LBM can be categorized as the generalized immersed boundary methods (IBM), including the diffuse- and sharp- interface IBM [18]. The diffuse-interface IBM employs the delta function for force spreading and velocity interpolation between Eulerian grids and Lagrangian boundary markers [7] as the classic IBM in Navier-Stokes (NS) solvers initially proposed by Peskin [19]. Moreover, some sharp-interface IBMs which extrapolates the fluid properties to virtual fluid node inside a solid, have also been developed for eliminating numerical slipping along the solid boundary [18]. Regarding the hydrodynamic force evaluation, the diffuse-interface IBM involves the integral of the boundary forces at Lagrangian solid nodes or Eulerian fluid nodes, while the stress integration method (SIM) and momentum exchange method (MEM) can be used for sharp-interface IBM and BB schemes [20]. SIM, originating from NS solvers, integrates stress and pressure along the fluid-solid interface. This implementation requires tedious extrapolation from fluid nodes to solid boundaries, potentially resulting in inefficiency and instability [13,20]. On the other hand, the hydrodynamic force calculation by MEM, inherited from kinetic theory, involves counting all momentum change between post-streaming and post-collision DFs along the links intersected with the solid boundary [20,21]. The conventional MEM violates local Galilean invariance, predicting an inaccurate hydrodynamic force in the moving frame of reference. To address this, Galilean-invariant momentum exchange method (GIMEM) is then proposed by Chen et al. [22] and Wen et al. [23], via introducing a solid velocity-related term into the momentum flux. Updating the position of structure relative to Eulerian grid, the refilling algorithm must then be implemented to construct the unknown DFs for fresh nodes uncovered from the solid, which generally includes the normal extrapolation, averaged extrapolation, and constructed non-equilibrium DFs [12]. Compared to these BCs, BB scheme and sharp-interface IBM methods must implement the refilling scheme for moving solids [7], while the diffuse-interface IBM does not require the refilling implementation and ensures mass conservation [18]. However, the diffuse-interface IBM is usually accompanied with a numerical slipping issue, resulting in a relatively lower accuracy with respect to interpolated bounce back (IBB) or sharp-interface IBM [13]. Overall, FSI approaches within LBM have been well validated to simulate immersed structures interacted with both laminar and turbulent single-phase flows [12,13,24–26].

When incorporating free surface flows into FSI problems, a significant challenge arises in accurately capturing the air-water interface. Within LBM, a sharp-interface approach, specifically the volume-of-fluid (VOF)-based method, proposed by Korner et al. [27] have been well-developed to stably and accurately capture the interface between two immiscible fluids with large density and viscosity ratios. This approach has gained considerable attention due to its computational efficiency for solving hydordynamic problems in civil and ocean enguneering, including applications of wave propagation [9,28], dam-break flows [29,30], hydraulic jump over a weir [31]. Korner's free surface model [27] discretises the advection equation of volume fraction using DFs, and it is a single-phase model in which the flow dynamics of gas phase are neglected and a free surface dynamic boundary condition is imposed to balance the hydrodynamic forces and surrounding gas pressure at the gas-liquid interface. Integrating the VOF and BB FSI approaches, for example, Thorimbert et al. [32] investigated wave interaction with a fixed oscillating water column WEC. Liu et al. [28] simulated water wave deformation over a submerged trapezoidal breakwater based on an improved dynamic-pressure LBM for resolving numerical energy dissipation and spurious currents. Janssen et al. [33] extended a hybrid LBM-FVM model to simulate dam-break flows interacting with stationary obstacles, combining LBM for flow field solution with piecewise linear interface reconstruction (PLIC)-VOF for capturing free surfaces. The dam-break flows were also simulated in a cumulant LBM model proposed by Sato et al. [29]. In addition to BB FSI approaches, Badarch et al. [34] applied the partially saturated method (PSM), a unique variant of diffuse-interface IBM [35], to predict wave loads on stationary vertical breakwaters in a VOF model. These studies primarily focused on stationary structures interacting with free surface flows, involving only phase state conversions between gas, liquid, and an intermediate interface state, inherent to the VOF method.

For moving structures interacting with free surface flows, an additional set of phase state conversion between solid and fluid must be addressed as required in FSI approaches. Xiao et al. [36] and Hao et al. [37] separately integrated IBM and BB approaches into the

VOF model to simulate a water exit case of an immersed cylinder. These studies validated the respective FSI implementations by comparing free surface elevation, wake vortex formation, and drag force on the cylinder. In such cases, the coupling interaction between moving immersed structures and free surface deformation is indirect, indicating that the FSI and VOF methods operate independently without requiring any modification. However, for partially submerged moving structures, numerical simulations become significantly more complex. These scenarios demand compatibility between two sets of phase state conversion rules related to transitions such as 'interface to solid', 'gas to solid', and 'liquid to solid', as shown in Fig. 1. Furthermore, appropriate boundary conditions must be implemented for the triple junctions where a computational cell simultaneously contains three phases: gas, liquid, and solid. To address these challenges, Xiao et al. [36] proposed an artificially filling interior domain algorithm for the application of diffuse-interface IBM in water entry of rigid bodies. Their approach involves filling the solid with virtual fluid and artificially adjusting the gas-liquid interface to ensure the structure is completely immersed in liquid, thereby allowing the FSI and VOF implementations to remain independent, as in the case of immersed structures. Liu et al. [38] combined a sharp-interface IBM, i.e., the ghost method, with VOF to model floating structures interacting with free surface flows. In addition to IBM [36,38], Bogner and Rüde [39] incorporated the BB methods into VOF model within LBM to track gas-liquid-solid interface. In their model, dynamic cell conversion rules were introduced to determine whether a previous solid cell should be converted into a gas, liquid, or interface state based on the neighbouring phase state. Hydrostatic stability cases in low-Reynolds-number flows were simulated to validate this model. Despite these advancements, Bogner and Rüde [39] reported significant challenges, including severe force fluctuations and spurious currents along solid boundaries, which were attributed to the limitations of refilling techniques and the effects of hydrostatic pressure gradients. These issues highlight the need for further refinement of the model to achieve accurate and stable simulations, particularly for complex dynamic scenarios and free surface flows at high Reynolds numbers.

As reviewed in the literature above, various FSI approaches have been extensively developed and applied to moving fully immersed structures [12,18,40]. However, simulating partially submerged moving structures in free surface flows remains scarce within the LBM framework. These scenarios involve complex phase state conversions and boundary condition implementations at the gas-liquid-solid interface, which are not yet fully addressed. Thus, the objective of this study is to develop an LBM framework for simulating partially submerged/floating structures in free surface flows, including hydrostatic and dynamic scenarios with special treatment for the triple junctions.

The remaining structure of this paper is organised as follows: Section 2 details the multi-relaxation-time (MRT) LBM model, free surface capturing method, fluid-structure interaction method, and numerical strategies for coupling VOF and FSI. Section 3 conducts six benchmark cases for model validation with increasing complexities. Finally, the conclusions are summarized in Section 4.

2. Numerical methods

A numerical model based on LBM is established for studying hydrodynamics of floating rigid bodies interacting with free surface flows, as sketched in Fig. 2. The single-phase VOF model [27] is implemented to capture the free surface. For fluid-structure interactions, the IBB is imposed at solid boundary for no-slip condition and the GIMEM is extended to hydrodynamic force evaluation of partially submerged bodies within the present modified-pressure LBM [28]. The numerical implementation of coupling fluid-structure-interaction and gas-liquid interface capturing are shown below.

2.1. MRT lattice Boltzmann equation

The continuous Boltzmann Equation with Bhatnagar-Gross-Krook (BGK) collision model [41] is expressed as,

$$\frac{\partial f}{\partial t} + \boldsymbol{e} \cdot \frac{\partial f}{\partial \boldsymbol{x}} + \mathscr{F} \cdot \frac{\partial f}{\partial \boldsymbol{e}} = -\frac{f - f^{\mathrm{eq}}}{\tau} \tag{1}$$

where $f(\boldsymbol{x}, \boldsymbol{e}, t)$ is the molecular distribution function at position $\boldsymbol{x}$ and time t for molecular velocity $\boldsymbol{e}$, and $\mathscr{F}$ is the external body force per unit mass; f^{eq} is the equilibrium distribution function and τ is the relaxation time. Ensuring conservation laws at the statistical or macroscopic level, it can be firstly discretised in the velocity space by Hermite series expansion [5]. The method of characteristics and

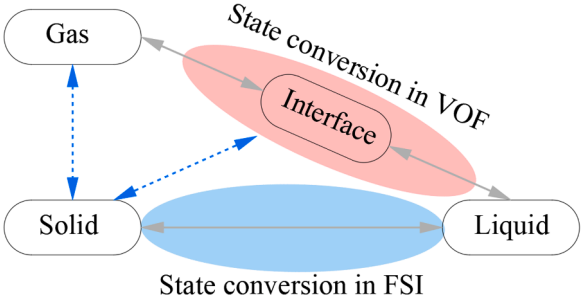

Fig. 1. Two sets of phase state conversions related to the VOF and FSI algorithms, the solid double-arrow lines denote the phase state conversion inherent in two algorithms, and dashed lines denote the additional conversion in coupling treatments algorithms for the present study.

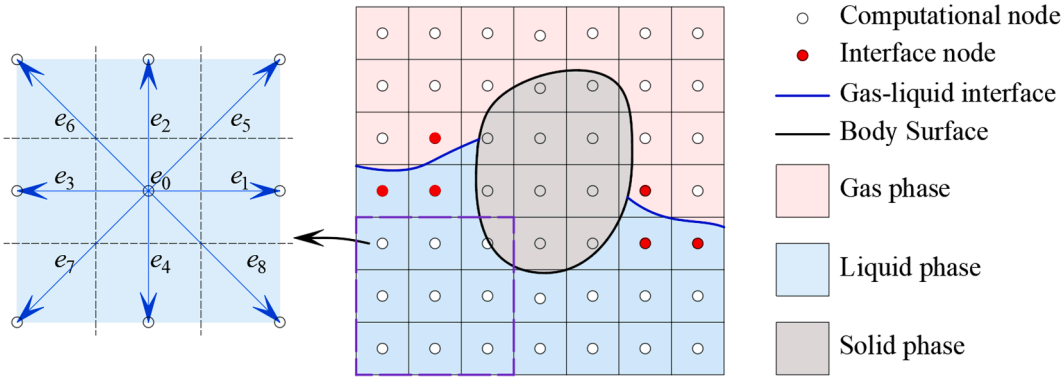

Fig. 2. Schematic diagram of floating structures in free surface flows with the D2Q9 lattice model.

trapezoidal time integration scheme can then be adopted to obtain the Lattice Boltzmann Equation (LBE) with second-order time and space accuracy [7]. The LBE with force or source term of Guo's scheme [42] is expressed as follows,

$$f_\alpha(\boldsymbol{x}+\boldsymbol{e}_\alpha\delta t, t+\delta t) - f_\alpha(\boldsymbol{x},t) = -\frac{\delta t}{\tau+0.5\delta t}\left(f_\alpha(\boldsymbol{x},t) - f_\alpha^{\mathrm{eq}}(\boldsymbol{x},t)\right) + \left(1-\frac{\delta t}{2\tau+\delta t}\right)\mathscr{F}_\alpha\delta t \tag{2}$$

in which f_α and $\mathscr{F}_\alpha$ are the discretised molecular distribution function $f(\boldsymbol{x},\boldsymbol{e},t)$ and force term $\mathscr{F}(\boldsymbol{x},\boldsymbol{e},t)$ in the α^{th} lattice direction with $\boldsymbol{e}_\alpha$ being discretised molecular velocity. δt and $\delta x = \sqrt{3}c_s\delta t$ are the time step and lattice spacing, respectively, $c_s = \sqrt{RT_0}$ is the sound speed where R and T_0 are the specific fluid constant and reference temperature. Various constructions of molecular structure, molecular velocities, and equilibrium distribution are available. The most popular lattice model in two-dimensional space is the D2Q9 model (nine velocities in two space dimensions), as shown in Fig. 2. The corresponding second-order equilibrium distribution functions f_α^{eq} and force term $\mathscr{F}_\alpha$ are expressed as,

$$\begin{aligned} f_\alpha^{\mathrm{eq}}(\boldsymbol{x},t) &= w_\alpha\rho\left[1+\frac{\boldsymbol{e}_\alpha\cdot\boldsymbol{u}}{c_s^2}+\frac{\boldsymbol{uu}\ :\ \left(\boldsymbol{e}_\alpha\boldsymbol{e}_\alpha - c_s^2\boldsymbol{I}\right)}{2c_s^4}\right] \\ \mathscr{F}_\alpha &= w_\alpha\rho\left[\frac{\boldsymbol{e}_\alpha\cdot\mathscr{F}}{c_s^2}+\frac{\boldsymbol{u}.\mathscr{F}\ :\ \left(\boldsymbol{e}_\alpha\boldsymbol{e}_\alpha - c_s^2\boldsymbol{I}\right)}{c_s^4}\right] \end{aligned} \tag{3}$$

where ρ and $\boldsymbol{u}$ are macroscopic density and velocity of the fluid; w_α is the weight coefficient; $\boldsymbol{I}$ is the identity tensor and the operator : denotes the double dot product. The macroscopic quantities, including density, velocity and stress tensor σ_{ij}, are evaluated from the velocity moments of f_α, as:

$$\begin{aligned} \rho &= \sum_\alpha f_\alpha \\ \rho u_i &= \sum_\alpha e_{\alpha i}\left(f_\alpha + \frac{\mathscr{F}_\alpha\delta t}{2}\right) \\ \sigma_{ij} &= \frac{2\tau}{2\tau+\delta t}\sum_\alpha e_{\alpha i}e_{\alpha j}\left(f_\alpha - f_\alpha^{\mathrm{eq}} + \frac{\mathscr{F}_\alpha\delta t}{2}\right) \end{aligned} \tag{4}$$

In single-relaxation-time model, these modes relax to equilibrium state with the same rate. In fact, inherited from kinetic theory, the various physical processes may relax with different transport coefficients. Such a model is termed as MRT LBM. The LBE in Eq. (2) is then rewritten as,

$$f_\alpha(\boldsymbol{x}+\boldsymbol{e}_\alpha\delta t, t+\delta t) - f_\alpha(\boldsymbol{x},t) = -\boldsymbol{M}^{-1}[\boldsymbol{S}(\boldsymbol{m}-\boldsymbol{m}^{\mathrm{eq}})] + \boldsymbol{M}^{-1}\left(\mathbf{I}-\frac{\boldsymbol{S}}{2}\right)\boldsymbol{\Phi}\delta t \tag{5}$$

$\boldsymbol{S} = \mathrm{diag}\left(1,\ \omega_e,\ \omega_\epsilon, 1,\ \omega_q, 1,\ \omega_q,\ \omega_\nu,\ \omega_\nu\right)$ is a relaxation matrix, where ω_e and $\omega_\nu = 1/(\tau/\delta t + 0.5)$ are related to bulk and shear viscosities, respectively; Within the assumption of low Mach number, ω_e, ω_ϵ and ω_q can be adjusted for numerical stability and accuracy. More details regarding the MRT-LBM model can be found in [7,28,43]. For the standard MRT model, nine independent modes in moment space for D2Q9 model are:

$$\boldsymbol{m} = \boldsymbol{M}f = \left(\rho, e, \epsilon, \rho u_x, q_x, \rho u_y, q_y, p_{xx},\ p_{xy}\right)^{\mathrm{T}} \tag{6}$$

where e and ϵ are connected to the kinetic energy and kinetic energy squared; $\boldsymbol{q}$ is related to the energy flux; p_{xx} and p_{xy} are related to the diagonal and non-diagonal components of the stress tensor. Corresponding to those moments, the transformation matrix ($\boldsymbol{M}$)

mapping distributions f_α to the moment space, the equilibrium moments $\boldsymbol{m}^{\mathrm{eq}} = \boldsymbol{M}f^{\mathrm{eq}}$, and force term in the moment space $\boldsymbol{\Phi} = \boldsymbol{M}\mathscr{F}$, can be expressed as, referring to the LBM model in [5,44],

$$\left\{\boldsymbol{M}_\alpha \quad \frac{\boldsymbol{m}^{\mathrm{eq}}}{\rho} \quad \frac{\boldsymbol{\Phi}}{\rho}\right\} = \begin{Bmatrix} 1 & 1 & 0 \\ \|\boldsymbol{e}_\alpha\|^2 - 4 & \|\boldsymbol{u}\|^2 - 2 & 2(\boldsymbol{\mathcal{F}}\cdot\boldsymbol{u}) \\ \frac{1}{2}\|\boldsymbol{e}_\alpha\|^4 - \frac{7}{2}\|\boldsymbol{e}_\alpha\|^2 + 4 & 1 - \|\boldsymbol{u}\|^2 & -2(\boldsymbol{\mathcal{F}}\cdot\boldsymbol{u}) \\ e_{\alpha,x} & u_x & \mathcal{F}_x \\ (\|\boldsymbol{e}_\alpha\|^2 - 5)e_{\alpha,x} & -u_x & -\mathcal{F}_x \\ e_{\alpha,y} & u_y & \mathcal{F}_y \\ (\|\boldsymbol{e}_\alpha\|^2 - 5)e_{\alpha,y} & -u_y & -\mathcal{F}_y \\ e_{\alpha,x}^2 - e_{\alpha,y}^2 & u_x^2 - u_y^2 & 2\left(\mathcal{F}_x u_x - \mathcal{F}_y u_y\right) \\ e_{\alpha,x}e_{\alpha,y} & u_x u_y & \mathcal{F}_y u_x + \mathcal{F}_x u_y \end{Bmatrix} \tag{7}$$

The present study applies the dynamic-pressure scheme that introduces the gravity $\boldsymbol{g}$ into pressure gradient term, to eliminate spurious current and energy dissipation which results from the inconsistency of gravity and pressure gradient [28]. Based on this modified-pressure LBM, the NSE can then be recovered from MRT-LBE through the Chapman-Enskog expansion [7] as follows,

$$\begin{aligned} &\frac{\partial\rho}{\partial t} + \frac{\partial(\rho u_i)}{\partial x_i} = 0 \\ &\frac{\partial\rho u_i}{\partial t} + \frac{\partial\left(\rho u_i u_j\right)}{\partial x_j} = -\frac{\partial p^*}{\partial x_i} + \frac{\partial}{\partial x_j}\left(\mu\left(\frac{\partial u_i}{\partial x_j} + \frac{\partial u_j}{\partial x_i}\right) + \left(\mu_{\mathrm{B}} - \frac{2\mu}{3}\right)\delta_{ij}\frac{\partial u_k}{\partial x_k}\right) + \rho\mathscr{F}_i \end{aligned} \tag{8}$$

with $p = \rho c_s^2$, shear viscosity $\mu = p\tau = p\left(\frac{\delta t}{\omega_v} - 0.5\delta t\right)$, bulk viscosity $\mu_{\mathrm{B}} = p\left(\frac{\delta t}{\omega_e} - 0.5\delta t\right) - \frac{\mu}{3}$ and $\mathscr{F}_i$ is the external force excluding gravity. $p^* = p - \rho_0\boldsymbol{g}(\boldsymbol{x} - \boldsymbol{x}_{\mathrm{ref}})$ is the dynamic pressure. This dynamic pressure scheme is also beneficial to correct the fluid forces highlighted by Bogner and Rüde [39] as the staircase approximated geometry description interacted with hydrostatic pressure gradient leads to inaccurate buoyancy force.

Free surface flows are typically characterized by high Reynolds numbers, making their turbulent nature computationally demanding to simulate accurately. To achieve a balance between the simulation detail and computational efficiency in practical numerical fluid simulations, this study employs the large eddy simulation (LES) approach integrated into the lattice Boltzmann framework, as proposed by Krafczyk et al. [45]. In the LES-LBE, turbulence modelling is based on a filtered lattice Boltzmann equation applied over a finite spatial region, resolving only turbulent structures larger than a specific sub-grid scale (SGS) length. The smaller turbulent structures, those below the filter length, are approximated using a simple turbulence closure model. In this framework, the total viscosity can be expressed as $\mu = \mu_{\mathrm{f}} + \mu_{\mathrm{t}}$ and the eddy viscosity is calculated by the magnitude of the mean strain rate tensor $\overline{\boldsymbol{S}}$,

$$\mu_{\mathrm{t}} = \rho(C_{\mathrm{s}}\delta)^2\|\,\overline{\boldsymbol{S}}\,\| = \rho(C_{\mathrm{s}}\delta)^2\frac{\|\,\overline{\boldsymbol{\sigma}}\|}{2\mu_{\mathrm{T}}} \tag{9}$$

where μ represents the total viscosity; μ_{f} is the fluid viscosity, which is 10^{-3} kg/(m·s) for water; and μ_{t} is the turbulent eddy viscosity. C_{s} is the Smagorinsky coefficient; $\delta = \delta_x$ is the filter length; and $\|\,\overline{\boldsymbol{\sigma}}\| = \sqrt{2\overline{\sigma}_{ij}\overline{\sigma}_{ij}}$. Substituting σ_{ij} in Eq. (4) into Eq. (9), it yields,

$$\tau = \frac{1}{2}\left(\tau_{\mathrm{f}} - 0.5\delta t\right) + \frac{1}{2}\sqrt{\left(\tau_{\mathrm{f}} + 0.5\delta t\right)^2 + \frac{2(C_s\delta)^2}{\rho c_s^4}\sqrt{2\widehat{\sigma}_{ij}\widehat{\sigma}_{ij}}} \tag{10}$$

where $\widehat{\sigma}_{ij} = \sum_\alpha e_{\alpha i}e_{\alpha j}\left(f_\alpha - f_\alpha^{\mathrm{eq}} + \frac{\mathscr{F}_\alpha\delta t}{2}\right)$.

The details of non-dimensional system can be found in [5,44].

2.2. Free surface capturing method

A sharp-interface approach, the volume-of-fluid method applicable to high-density ratio fluid flows, is extensively applied in NS-based solvers and is recently introduced to LBM by Korner et al. [27]. Korner et al. [27] assumes that the heavier phase completely dominates the flow dynamic of two immiscible fluids. This system reduces to a single-phase flow model with a free surface boundary. The lighter phase thus neither contains DFs nor participate in the LBM evolution. To determine the phase state of the local cell, a volume fraction ε is defined as the ratio of liquid volume and fluid-accessible volume, as follows

$$\varepsilon(\boldsymbol{x}, t) = \frac{V_{\mathrm{liquid}}}{V - V_{\mathrm{solid}}} = \frac{m(\boldsymbol{x}, t)}{\varphi(\boldsymbol{x}, t)\rho(\boldsymbol{x}, t)\delta x^2} \tag{11}$$

where m and ρ are the mass and density of liquid phase, respectively; $\varphi(\boldsymbol{x},t)=1-\varepsilon_s$ is the porosity and ε_s is the solid fraction $\varepsilon_s = V_s/\delta x^2$. Concerning floating solids in free surface flows, a cell may be occupied by gas, liquid and solid phases at the same moment, so the concept of porosity and solid fraction is introduced here. For convenience of numerical implementation, a phase state function $s(\boldsymbol{x},t)$ is defined in present single-phase model according to the fluid fraction,

$$s(\boldsymbol{x},t)=\begin{cases}\text{gas} & \varepsilon(\boldsymbol{x},t)=0\\ \text{interface} & 0<\varepsilon(\boldsymbol{x},t)<1\\ \text{liquid} & \varepsilon(\boldsymbol{x},t)=1\end{cases} \tag{12}$$

In this VOF-LBM method, the free surface movement is governed by the advection equation of the liquid mass of interface cells, as follows,

$$\frac{\partial\rho}{\partial t}+\nabla\cdot(\rho\boldsymbol{u})=0 \tag{13}$$

Integrating this equation over the control cell and applying the divergence theorem to convert the convective term to a surface integral, it can be discretised using first-order explicit Euler time difference scheme as follows,

$$m(\boldsymbol{x},t+\delta t)=m(\boldsymbol{x},t)+\delta t\sum_{\alpha}\psi_{\alpha} \tag{14}$$

where ψ_α is the liquid flux in the α^{th} direction in the present LBM system and computed from the LBM streaming step as,

$$\delta t\psi_{\alpha}(\boldsymbol{x},t)=\left(f^{*}_{\bar{\alpha}}(\boldsymbol{x}+\boldsymbol{e}_{\alpha}\delta t,t)-f^{*}_{\alpha}(\boldsymbol{x},t)\right)A_{\alpha}\,\delta x \tag{15}$$

where $\boldsymbol{e}_{\bar{\alpha}}=-\boldsymbol{e}_{\alpha}$; f^{*}_{α} is the post-collision DF; and A_α denotes the face fill level determined by

$$A_{\alpha}=\begin{cases}0 & s(\boldsymbol{x}+\boldsymbol{e}_{\alpha}\delta t)=\text{gas}\\ \dfrac{\varepsilon(\boldsymbol{x})\varphi(\boldsymbol{x})+\varepsilon(\boldsymbol{x}+\boldsymbol{e}_{\alpha}\delta t)\varphi(\boldsymbol{x}+\boldsymbol{e}_{\alpha}\delta t)}{2}\delta x & s(\boldsymbol{x}+\boldsymbol{e}_{\alpha}\delta t)=\text{interface}\\ \dfrac{\varphi(\boldsymbol{x})+\varphi(\boldsymbol{x}+\boldsymbol{e}_{\alpha}\delta t)}{2}\delta x & s(\boldsymbol{x}+\boldsymbol{e}_{\alpha}\delta t)=\text{liquid}\end{cases} \tag{16}$$

In this formulation, for an interface cell at $\boldsymbol{x}$, first and third conditions indicate that the face between $\boldsymbol{x}$ and $\boldsymbol{x}+\boldsymbol{e}_{\alpha}\delta t$ is considered completely dry or fully submerged, respectively, depending on whether the neighbouring cell is identified as gas or liquid. The second condition corresponds to a neighbouring interface cell, for which partial submergence is determined based on the average volume fraction.

This is a single-phase model without solving LBE at the gas phase, and a free surface boundary condition needs to be implemented to recover atmospheric pressure at gas-liquid interface. Those missing distributions streaming from gas phase with invalid information are reconstructed by the free surface dynamic boundary condition originally proposed by Korner et al. [27] (FSK),

$$f_{\bar{\alpha}}(\boldsymbol{x},t+\delta t)=-f^{*}_{\alpha}(\boldsymbol{x},t)+f^{\text{eq}}_{\alpha}(\rho_{\text{G}},\boldsymbol{u}_{\text{G}})+f^{\text{eq}}_{\bar{\alpha}}(\rho_{\text{G}},\boldsymbol{u}_{\text{G}}) \tag{17}$$

where $\boldsymbol{u}_{\text{G}}$ is the free surface velocity extrapolated from liquid nodes. In modified-pressure LBM, surrounding atmospheric pressure ρ_{G} is expressed as $\rho_{\text{G}}=\rho_0-\rho_0\boldsymbol{g}(\boldsymbol{x}-\boldsymbol{x}_{\text{ref}})/c_s^2$, instead.

After the mass exchange and DFs reconstruction are completed, the liquid fraction ε can be updated by Eq. (11). An interface cell will finally be converted to gas or liquid cell when it gets empty, $\varepsilon(\boldsymbol{x},t+\delta t)<0-\delta\varepsilon$, or filled, $\varepsilon(\boldsymbol{x},t+\delta t)>1+\delta\varepsilon$, where $\delta\varepsilon$ is a conversion threshold designed to prevent oscillatory transitions, set to 0.001 following the value commonly used in existing literature (see [27,39]). A liquid cell cannot be converted a gas cell directly and vice versa. When the neighbour of a gas (or liquid) cell gets filled (or empty), the gas (or liquid) cell itself must be converted to an interface cell to maintain a closed interface layer to separate the liquid and gas phase. In addition, to alleviate the unphysical bubble and spatter, interface cells are also identified as different node quality: standard, no-air neighbour, no-liquid neighbour. For the interface cell at $\boldsymbol{x}$ that has no gas neighbour, it obtains more mass from neighbouring interface cells, while the interface cell at $\boldsymbol{x}$ that has no liquid neighbour, loses more mass, as suggested in [10,27].

We do not modify the DFs when liquid cells are converted to the interface cell, and vice versa. In contrast, when a gas cell is converted to an interface cell, its DFs need to be initialized because the gas cell has no valid information in the present single-phase model. The DFs are initialized by equilibrium DFs as expressed in Eq. (3), in which the macroscopic quantities are extrapolated from neighbouring liquid and interface cells as follows,

$$\overline{\varphi}(\boldsymbol{x})=\frac{\sum_{\alpha\in\mathscr{J}}w_{\alpha}\varphi(\boldsymbol{x}+\boldsymbol{e}_{\alpha}\delta t)}{\sum_{\alpha\in\mathscr{J}}w_{\alpha}},\mathscr{J}_1=\{\alpha|s(\boldsymbol{x}+\boldsymbol{e}_{\alpha}\delta t)=\text{liquid},\ \text{interface}\} \tag{18}$$

The volume fraction of an empty or filled cell is set to $\varepsilon(\boldsymbol{x},t)=0$ or $\varepsilon(\boldsymbol{x},t)=1$ following the state conversion, respectively, which causes an excess mass m^{ex} of,

$$m^{\mathrm{ex}} = \begin{cases} m - \rho(\boldsymbol{x},t) & s(\boldsymbol{x}) \text{ gets filled} \\ m & s(\boldsymbol{x}) \text{ gets empty} \end{cases} \tag{19}$$

Concerning the mass conservation, interface and new-interface cells need to accept the excess mass allocated from surrounding empty ($\varepsilon < 0$) and filled ($\varepsilon > 1$) cells. In present study, the normal direction-based algorithm is applied as suggested in [27]. More details regarding the free surface model can be found in [27,30,39].

It should be noted that an empty or filled cell must be marked as a transmitted state before allocating excess mass to ensure consistency in parallel computing. The free surface algorithm described above guarantees exclusive memory access at each thread during parallel computing, not involving non-local write operations in mass allocation and state conversion. In addition, the Weber number of each test case in this work is significantly greater than 1, indicating that surface tension effect is negligible and thus is not included.

2.3. Fluid-Structure interaction method

For modelling the motion of the rigid bodies interacting with fluid flows, it requires addressing three aspects of numerical implementations: the no-slip fluid-solid boundary condition, the hydrodynamic force evaluations and the initialization for new-born fluid nodes. To facilitate the description of liquid-solid dynamics, the cell type of solid is incorporated into the phase state function $s(\boldsymbol{x}, t)$, extending its representation beyond gas-liquid interactions,

$$s(\boldsymbol{x},t) = \begin{cases} \text{solid}, \ \boldsymbol{x} \in \Omega_{\text{solid}} \\ \text{fluid} \begin{cases} \text{gas} & \varepsilon(\boldsymbol{x},t) = 0 \\ \text{interface} & 0 < \varepsilon(\boldsymbol{x},t) < 1 \\ \text{liquid} & \varepsilon(\boldsymbol{x},t) = 1 \end{cases} \end{cases} \tag{20}$$

where Ω_{solid} represents the solid region.

For a fluid node at the position $\boldsymbol{x}$, the unknown DFs streaming from the solid need to be reconstructed to satisfy the no-slip and impermeable boundary conditions. If the node along the opposite direction at $\boldsymbol{x} + \boldsymbol{e}_{\bar{\alpha}}\delta t$ has valid fluid information, the united interpolated bounce back (UIBB) scheme is imposed,

$$\begin{cases} f_{\bar{\alpha}}(\boldsymbol{x}, t+\delta t) = \dfrac{q f_{\alpha}^{*}(\boldsymbol{x},t) + q f_{\bar{\alpha}}^{*}(\boldsymbol{x},t) + (1-q) f_{\alpha}^{*}(\boldsymbol{x}+\boldsymbol{e}_{\bar{\alpha}}\delta t, t) - 2 w_{\alpha}\rho_{\mathrm{w}}\boldsymbol{e}_{\alpha}\cdot\boldsymbol{u}_{\mathrm{w}}}{1+q} & s(\boldsymbol{x}+\boldsymbol{e}_{\bar{\alpha}}\delta t) = \text{liquid, interface} \\ f_{\bar{\alpha}}(\boldsymbol{x}, t+\delta t) = \dfrac{f_{\alpha}^{*}(\boldsymbol{x},t) + q f_{\bar{\alpha}}^{*}(\boldsymbol{x},t) - 2 w_{\alpha}\rho_{\mathrm{w}}\boldsymbol{e}_{\alpha}\cdot\boldsymbol{u}_{\mathrm{w}}}{1+q} & \text{otherwise} \end{cases} \tag{21}$$

where the relative distance q is defined as $q = |\boldsymbol{x} - \boldsymbol{x}_{\mathrm{w}}|/|\boldsymbol{e}_{\alpha}\delta t|$, $\boldsymbol{u}_{\mathrm{w}}$ is the solid boundary velocity at $\boldsymbol{x}_{\mathrm{w}}$ and ρ_{w} is the fluid density at solid boundary, estimated as the nearest local liquid density $\rho(\boldsymbol{x}, t)$ (i.e., using constant extrapolation), in the present nearly incompressible flows.

The momentum change of DFs (between post-collision$f_{\alpha}^{*}(\boldsymbol{x}, t)$ and post-streaming $f_{\bar{\alpha}}(\boldsymbol{x}, t+\delta t)$) denotes the discrete net force acted on solid in the MEM. Peng et al. [12] compared different MEM methods and pointed out the GIMEM ensures the local Galilean invariance and partially reduces unphysical force fluctuation when implementing IBB scheme at moving fluid-solid boundary. Therefore, GIMEM is applied in the present study, as:

$$\begin{cases} \boldsymbol{F}_{\bar{\alpha}}(\boldsymbol{x}, t+\delta t) = -\dfrac{\delta x^2}{\delta t}\left(f_{\bar{\alpha}}(\boldsymbol{x}, t+\delta t)(\boldsymbol{e}_{\bar{\alpha}} - \boldsymbol{u}_{\mathrm{w}}) - f_{\alpha}^{*}(\boldsymbol{x}, t)(\boldsymbol{e}_{\alpha} - \boldsymbol{u}_{\mathrm{w}})\right) \\ \boldsymbol{M}_{\bar{\alpha}}(\boldsymbol{x}, t+\delta t) = \boldsymbol{F}_{\bar{\alpha}}(\boldsymbol{x}, t+\delta t)(\boldsymbol{x}_{\mathrm{w}} - \boldsymbol{R}) \end{cases} \tag{22}$$

Where $\boldsymbol{F}_{\bar{\alpha}}$ and $\boldsymbol{M}_{\bar{\alpha}}$ denote the discrete net force and torque at $\boldsymbol{x}_{\mathrm{w}}$, respectively; $\boldsymbol{e}_{\alpha}$ is the discrete velocity pointed to solid nodes; $\boldsymbol{x}_{\mathrm{w}}$ is the intersection of $\boldsymbol{e}_{\alpha}$ links and solid boundary; and $\boldsymbol{R}$ is the rotational center.

For a fully immersed structure, the contribution of atmospheric pressure to the hydrodynamic forces cancels out. However, for a floating one, we need to get rid of the effect of absolute atmospheric pressure and take hydrostatic pressure gradient into account in the present modified-pressure LBM model. One correction introducing the equilibrium distribution function $f_{\alpha}^{\mathrm{eq}}(\rho_{\mathrm{G,w}}, \ \boldsymbol{u}_{\mathrm{w}})$ into GIMEM can eliminate the contribution of absolute atmospheric pressure and correctly evaluate the hydrostatic buoyancy as,

$$\begin{cases} \boldsymbol{F}_{\bar{\alpha}} = -\varepsilon\dfrac{\delta x^2}{\delta t}\left(\left(f_{\bar{\alpha}}(\boldsymbol{x}, t+\delta t) - f_{\bar{\alpha}}^{\mathrm{eq}}\right)(\boldsymbol{e}_{\bar{\alpha}} - \boldsymbol{u}_{\mathrm{w}}) - \left(f_{\alpha}^{*}(\boldsymbol{x}, t) - f_{\alpha}^{\mathrm{eq}}\right)(\boldsymbol{e}_{\alpha} - \boldsymbol{u}_{\mathrm{w}})\right) \\ \quad or \ \boldsymbol{F}_{\bar{\alpha}} = -\dfrac{\delta x^2}{\delta t}\left(f_{\bar{\alpha}}(\boldsymbol{x}, t+\delta t)(\boldsymbol{e}_{\bar{\alpha}} - \boldsymbol{u}_{\mathrm{w}}) - f_{\alpha}^{*}(\boldsymbol{x}, t)(\boldsymbol{e}_{\alpha} - \boldsymbol{u}_{\mathrm{w}})\right) + \boldsymbol{F}_{\bar{\alpha},\mathrm{H}} \\ \boldsymbol{M}_{\bar{\alpha}} = \boldsymbol{F}_{\bar{\alpha}}(\boldsymbol{x}_{\mathrm{w}} - \boldsymbol{R}) \end{cases} \tag{23}$$

where $\rho_{\mathrm{G,w}} = \rho_0 - \rho_0\boldsymbol{g}\left(\boldsymbol{x}_{\mathrm{w}} - \boldsymbol{x}_{\mathrm{ref}}\right)/c_s^2$ and $\boldsymbol{F}_{\bar{\alpha},\mathrm{H}} = \varepsilon\frac{\delta x^2}{\delta t}\left(f_{\bar{\alpha}}^{\mathrm{eq}}\ (\boldsymbol{e}_{\bar{\alpha}} - \boldsymbol{u}_{\mathrm{w}}) - f_{\alpha}^{\mathrm{eq}}(\boldsymbol{e}_{\alpha} - \boldsymbol{u}_{\mathrm{w}})\right)$.

Then the total hydrodynamic forces and torque acting on the object are summed as,

$$\begin{cases} \boldsymbol{F} = \sum\limits_{\mathrm{G}(\boldsymbol{x})} \sum\limits_{\alpha \in \mathscr{S}_2} \boldsymbol{F}_{\bar{\alpha}}(\boldsymbol{x}, t+\delta t) \\ \boldsymbol{M} = \sum\limits_{\mathrm{G}(\boldsymbol{x})} \sum\limits_{\alpha \in \mathscr{S}_2} \boldsymbol{M}_{\bar{\alpha}}(\boldsymbol{x}, t+\delta t) \end{cases}, \mathscr{S}_2 = \{\alpha | s(\boldsymbol{x} + \boldsymbol{e}_\alpha \delta t) = \text{solid}\} \tag{24}$$

where $\mathrm{G}(\boldsymbol{x})$ denotes the set of non-solid nodes which directly link to solid nodes. When the hydrodynamic force and torque are known, the accelerations are calculated according to the motion equation of the rigid body and then the velocity and position are updated implementing forward Euler or Runge-Kutta second-order time integration scheme.

$$\begin{cases} m_\mathrm{s} \dfrac{d\boldsymbol{u}_\mathrm{s}}{dt} = \boldsymbol{F} + m_\mathrm{s}\boldsymbol{g} \\ I_\mathrm{s} \dfrac{d\boldsymbol{\omega}_\mathrm{s}}{dt} + \boldsymbol{\omega}_\mathrm{s} \times I_\mathrm{s}\boldsymbol{\omega}_\mathrm{s} = \boldsymbol{M} + m_\mathrm{s}(\boldsymbol{x}_\mathrm{m} - \boldsymbol{x}_\mathrm{s}) \times \boldsymbol{g} \end{cases} \tag{25}$$

where $\boldsymbol{x}_\mathrm{s}$ and $\boldsymbol{x}_\mathrm{m}$ denote the position vectors of rotational center and mass center, respectively; m_s and I_s are the mass and moment of inertia; $\boldsymbol{u}_\mathrm{s}$ and $\boldsymbol{\omega}_\mathrm{s}$ is the velocity and angular velocity. Once the motion equation above is solved, the solid position and surface velocity can be updated by,

$$\begin{aligned} \frac{d\boldsymbol{x}_\mathrm{s}}{dt} &= \boldsymbol{u}_\mathrm{s} \\ \boldsymbol{u}_p &= \boldsymbol{u}_\mathrm{s} + \boldsymbol{\omega}_\mathrm{s} \times (\boldsymbol{x} - \boldsymbol{x}_\mathrm{s}) \end{aligned} \tag{26}$$

As stated by Bogner and Rüde [39], hydrodynamic force errors are partially attributed to the hydrostatic density gradient interacted with the inaccurate geometric description for the solid boundary. It can be reduced by a sub-grid method for the hydrostatic pressure field on present modified-pressure LBM. In sub-grids, the equilibrium DFs based on hydrostatic pressure is $f^{\mathrm{eq}}_{\alpha,\mathrm{sub}} = f^{\mathrm{eq}}_{\alpha}\left(\rho_{\mathrm{G,w,sub}}, \boldsymbol{u}_{\mathrm{w,sub}}\right)$ where $\rho_{\mathrm{G,w,sub}} = \rho_0 - \rho_0 \boldsymbol{g}\left(\boldsymbol{x}_{\mathrm{w,sub}} - \boldsymbol{x}_{\mathrm{ref}}\right)/c_s^2$. The hydrostatic buoyancy force $\boldsymbol{F}_{\alpha,\mathrm{H}}$ in each grid cell can then be calculated by,

$$\boldsymbol{F}_{\bar{\alpha},\mathrm{H}} = \sum_{\alpha,\mathrm{sub}\to\mathrm{solid}} \varepsilon \frac{\delta x^2}{n\delta t} \left(\left(f^{\mathrm{eq}}_{\bar{\alpha},\mathrm{sub}} \right) \left(\boldsymbol{e}_{\bar{\alpha},\mathrm{sub}} - \boldsymbol{u}_{\mathrm{w,sub}} \right) - \left(f^{\mathrm{eq}}_{\alpha,\mathrm{sub}} \right) \left(\boldsymbol{e}_{\alpha,\mathrm{sub}} - \boldsymbol{u}_{\mathrm{w,sub}} \right) \right) \tag{27}$$

where n denotes the sub-grid spacing is $\delta x/n$; $\boldsymbol{e}_{\alpha,\mathrm{sub}}$ is the lattice link between liquid sub-grid and solid sub-grid, and $\boldsymbol{u}_{\mathrm{w,sub}}$ is velocity at solid boundary $\boldsymbol{x}_{\mathrm{w,sub}}$ intersected with the lattice link, as shown in Fig. 3. Similar modification is carried out for the torque $\boldsymbol{M}_{\bar{\alpha},\mathrm{H}}$.

Following the update of solid position and velocity, new-born liquid or interface cells must be initialized as previous solid cells have no valid DFs, known as the refilling scheme. The average density of surrounding liquid or interface nodes is used as the initialized density. The initialized velocity can be the closest solid boundary velocity or local average value. Then the DFs are reconstructed as the equilibrium distribution functions $f_\alpha(\boldsymbol{x}, t+\delta t) = f^{\mathrm{eq}}_\alpha\left(\rho_{\mathrm{avg}}, \boldsymbol{u}_{\mathrm{avg}}\right)$ as Eq. (3). Such a refilling scheme without non-equilibrium term may result in the severe force fluctuation and we hence use the consistent initial condition presented by Mei et al. [46] and Chen et al. [18]. It is an iteration process: the equilibrium DFs and macroscopic variables above are used as the initial input for those fresh nodes, then

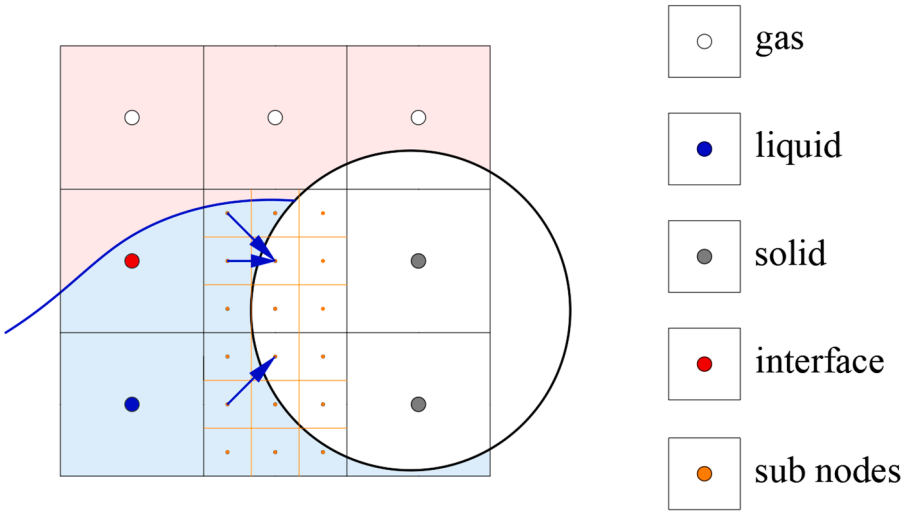

Fig. 3. Local sub-grids schematic. The blue arrows denote the links $\boldsymbol{e}_{\alpha,sub}$ of sub-liquid nodes to solid, and the solid blue line is the gas-liquid interface.

the collision is carried out at the fresh nodes and streaming is carried out at fresh nodes as well as surrounding liquid and interface nodes, as,

$$f_\alpha^*(\boldsymbol{x},t) = f_\alpha(\boldsymbol{x},t) - \boldsymbol{M}^{-1}[\boldsymbol{S}(\boldsymbol{m}-\boldsymbol{m}^{\mathrm{eq}})] + \boldsymbol{M}^{-1}\left(\mathbf{I}-\frac{\boldsymbol{S}}{2}\right)\boldsymbol{\Phi}\delta t,\ s(\boldsymbol{x}) \in \text{fresh cells} \tag{28a}$$

$$f_\alpha(\boldsymbol{x}+\boldsymbol{e}_\alpha\delta t, t+\delta t) = f_\alpha^*(\boldsymbol{x},t),\ s(\boldsymbol{x}) \in \text{fresh cells and surrounding valid cells} \tag{28b}$$

The iteration will end if a stable density field at those fresh nodes reaches the following condition,

$$\sum_{\boldsymbol{x}} \frac{|\rho(t+\delta t)-\rho(t)|}{|\rho(t+\delta t)+\rho(t)|} < \delta \tag{29}$$

where δ is a tiny quantity as the convergence criterion, set to 10^{-8}.

2.4. Coupling treatments of VOF and FSI

The gas-liquid interface has been built meticulously using the single-phase VOF model. When mapping solid to the fluid grids, it must ensure the interface to separate liquid from gas. Referring to Bogner and Rüde [39], a set of phase state conversion rules dependent on neighbouring node states (liquid, interface, or gas) is implemented to address this issue. Such dependence requires tiny motion of solid during a time step so that the cell state conversion occurs at solid and fluid nodes which directly link to each other. Destruction is straightforward and generally safe, i.e., fluid types to the solid types. However, inappropriate creation may cause damaged gas-liquid interface. The solid nodes at present time step, which are to be uncovered at next time step, are identified for updating as follows,

1. A node having no liquid neighbour is marked as 'SolidToGas' node as shown in light grey in Fig. 4;
2. A node having no gas neighbour is marked as 'SolidToLiquid' node as shown in light blue in Fig. 4;
3. A node having both gas and liquid neighbours is marked as 'SolidToInterface' node as shown in pink.

Similar to the numerical implementation in free surface algorithms, certain transmitted states (SolidToLiquid, SolidToGas and SolidToInterface) are also introduced for ensuring consistency of parallel computing. After initialization for those uncovered nodes, they are then converted into liquid, gas, and interface, respectively.

It should be noted that the green node is unable to be determined according to the rules described above if the solid has large motion. In fact, the small-motion assumption can be naturally satisfied for the simulation with low Mach number. if the TBD node exists, it means the velocity of object exceeds $\sqrt{3RT_0}$, violating the requirement of low Ma number.

The algorithm described so far can be implemented to track the gas-liquid-solid interface. However, one unphysical phenomenon occurs where the solid perturbs liquid before actual contact and the liquid always adheres to the solid surface. One reason is that the mass change of interface cell depends on neighbouring cell states in the present free surface model. As illustrated in Fig. 5, although the solid has not penetrated the gas-liquid interface, the pink interface node identified as 'no-gas neighbour' gains more mass from surrounding interface cells marked 'standard'. The second reason is that such dependency on neighbouring node states also exists on hydrodynamic force evaluations as the blue link between interface and 'GasToSolid' nodes shown in Fig. 5. According to Eq. (24), the liquid unphysically exerts hydrodynamic force to solid at this moment.

To effectively mitigate the spurious currents, the following identifications are incorporated into the gas-liquid-solid model above. When the neighbour ($\boldsymbol{x}+\boldsymbol{e}_\alpha\delta t$) of an interface node is a solid node,

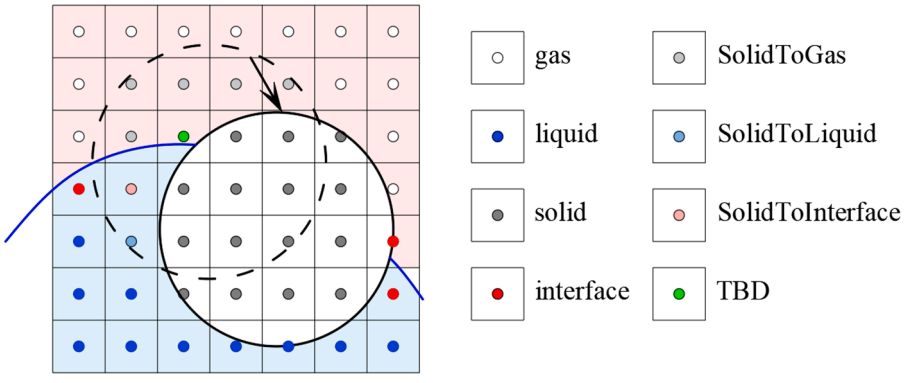

Fig. 4. Cell states conversion after the rigid object moves. The solid and dashed black lines denote the object boundary at new moment and old moment separately, the green node (TBD) indicates a cell whose state is to be determined, and the solid blue line is the gas-liquid interface.

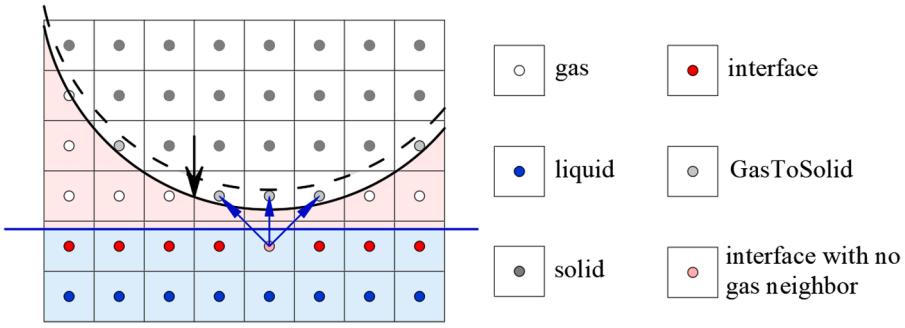

Fig. 5. Node quality changes when neighbouring gas cells are converted to solid cells. The solid and dashed black lines separately denote the object boundary at new moment and old moment, and the solid blue line is the gas-liquid interface.

1. $\boldsymbol{n} \cdot \boldsymbol{e}_\alpha > 0$: the solid node is located outside the gas-liquid interface and the solid node is regarded as a gas node when we identify the node quality at $\boldsymbol{x}$, as the light grey in Fig. 6, where $\boldsymbol{n}$ is the outward normal direction at the interface cell.
2. $\boldsymbol{n} \cdot \boldsymbol{e}_\alpha < 0$: the solid node is located inside the gas-liquid interface and the solid node is regarded as a liquid node when we identify the node quality at $\boldsymbol{x}$;

   For convenience, the above rules are called as 'node quality identification method' (NQIM) rules.
3. $f_{\bar{\alpha}}(\boldsymbol{x}, t+\delta t)$ with $\boldsymbol{n} \cdot \boldsymbol{e}_\alpha > 0$ is reconstructed by free surface scheme FSK in this link, instead. Correspondingly, this link should be removed from $\mathrm{G}(\boldsymbol{x})$ in Eq. (24) evaluating hydrodynamic forces. One case is presented in Fig. 6, in which those black arrows denote their opposite $f_{\bar{\alpha}}(\boldsymbol{x}, t+\delta t)$ are reconstructed by IBB and blue ones represent the FSK scheme is imposed. It is critical to ensure that the solid is not surrounded by gas and interface nodes. This rule for an interface cell which also contains gas and solid phases is called as 'boundary conditions identification method' (BCIM) rule.

The entire framework coupling VOF and IBB-GIMEM for simulating floating rigid bodies in free surface flows is concluded as follows:

Fig. 7

3. Model validation

To validate the developed 2D LBM model for simulating the floating structures in free surface flows, the validation procedure is organised progressively as follows: (1) submerged structures interacted with single-phase flows, (2) stationary submerged and floating structures in free surface flows, (3) submerged structures interacted with free surface flows, (4) partially submerged stationary structures interacted with free surface flows, (5) partially submerged structures with single degree of freedom in free surface flows, and (6) freely floating structures interacted with water waves.

3.1. Free settling of an immersed solid

The first benchmark evaluates a submerged structure interacting with single-phase flows without a free surface, aiming to verify the accuracy of FSI algorithm and the proposed method for hydrostatic buoyancy evaluations. The benchmark case chosen involves an immersed cylinder freely-settling in a vertical channel [12,23]. As shown in Fig. 8, the channel has a width of $4D$ and a length of $25D$, where D represents the cylinder diameter. The cylinder diameter D is 0.1 cm, and its density ρ_s is 1.03 times the fluid density ρ_0. The cylinder initially positioned 0.076 cm relative to the left wall, is released to translate and rotate under its own weight and the fluid forces. The kinematic viscosity of fluid is 0.01 cm^2/s and gravity acceleration is set as 980 cm/s^2. The relaxation coefficients of

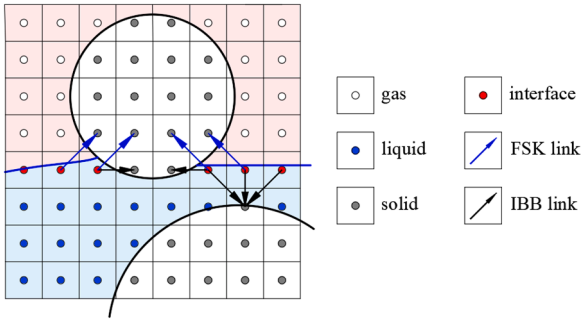

Fig. 6. Implementation of boundary conditions for those interface nodes linking to solid nodes according to the rules.

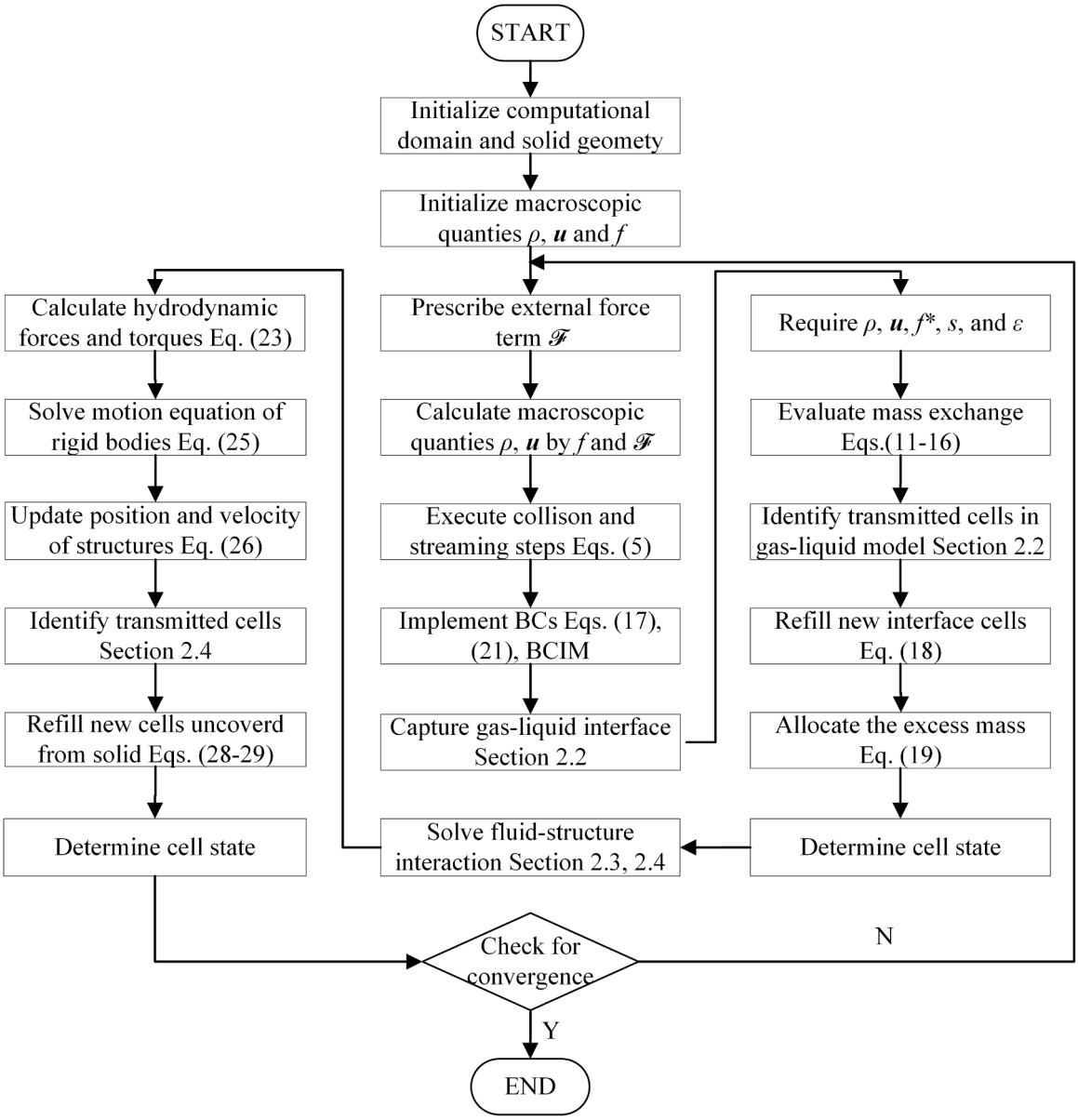

Fig. 7. Flow chart of gas-liquid-solid model within the dynamic-pressure LBM.

single-phase flows are chosen as them used in [12,23] for the purpose of reproducibility, i.e., $\boldsymbol{S} = \mathrm{diag}(1,\ 1.64,\ 1.54,1,\ 1.9,1,\ 1.9,\ \omega_\nu,\ \omega_\nu)$. No-slip BCs are applied to the left and right wall boundaries, while periodic BCs are used for top and bottom boundaries. The lattice grid resolution is set as $D/30$. Figs. 9 shows the time histories of center trajectory, velocities and hydrodynamic forces where gravity is not involved in the numerical simulation and the hydrostatic buoyancy is theoretically given. It is observed that the asymmetric flow field causes the cylinder to drift toward the vertical centerline of the channel, eventually reaching a steady state characterized by a constant vertical settling velocity. The numerical results exhibit excellent agreement with those reported by Wen et al. [23], thereby validating the accuracy and reliability of the present model for simulating fluid-structure interactions involving immersed bodies.

Unlike fully immersed objects, the hydrostatic buoyancy F_H and M_H of a partially submerged object is dependent on the submerged depth and thus cannot be theoretically determined. To validate the proposed method for calculating buoyancy, as expressed in Eq. (27), Fig. 10 presents the comparison of total fluid forces and torque between cases where hydrostatic buoyancy is numerically evaluated and theoretically prescribed. The case of n =1 represents a scenario without the sub-grid system while the dashed line corresponds to a numerical simulation in which the gravity is not involved and the hydrostatic buoyancy is theoretically determined. The total fluid forces computed with numerical hydrostatic buoyancy exhibit fluctuations around the results obtained when F_H and M_H are set to their theoretical values. As expected, force fluctuations resulting from the hydrostatic pressure gradient significantly

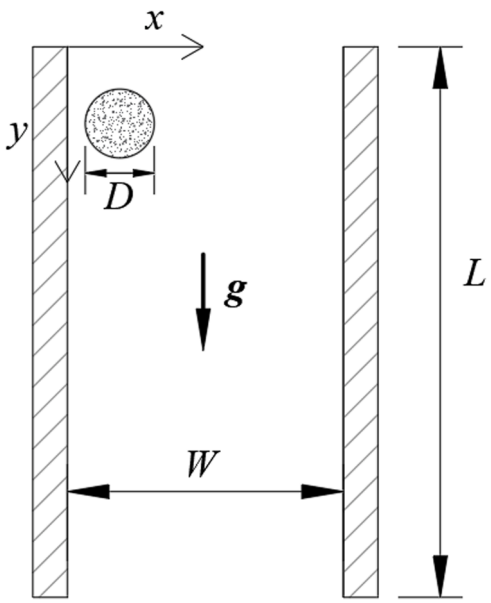

Fig. 8. A schematic diagram of cylinder sedimentation in a vertical channel, where $\boldsymbol{g}$ is the gravity; W and L are the channel width and height respectively.

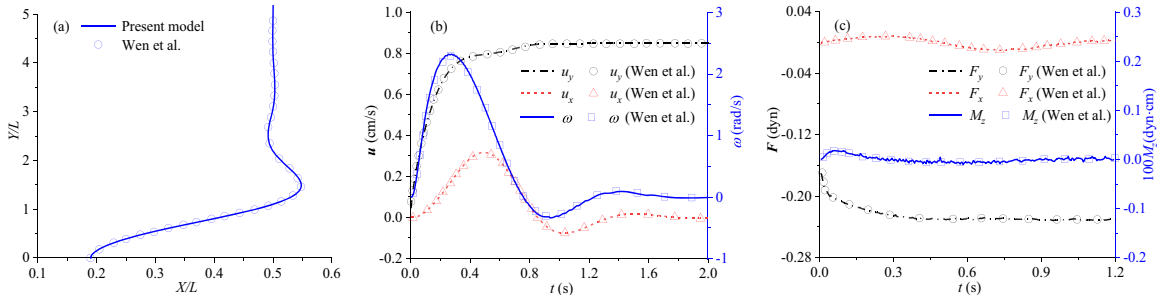

Fig. 9. Time evolution of position, velocities, and forces of the circular cylinder during freely settling, compared with them of Wen et al. [23]. (a) Centroid trajectories, (b) velocities, and (c) acting forces.

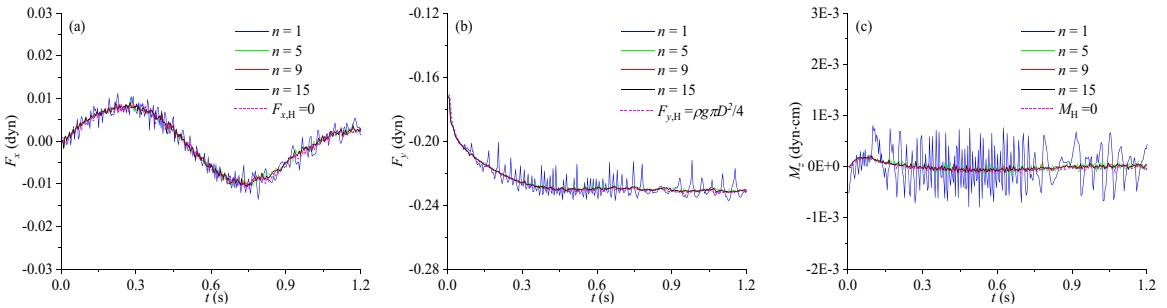

Fig. 10. Time evolution of hydrodynamic forces with different sub-grid refinement n=1, 5, 9 and 15. (a) horizontal force F_x, (b) vertical force F_y and (c) torque M_z.

diminish with increasing refinement levels. These results demonstrate that the developed force evaluation method within the modified-pressure LBM is feasible to calculate the hydrostatic buoyancy and the sub-grid technique can effectively alleviate the force error induced by hydrostatic pressure gradient.

3.2. Static buoyant circular cylinder

To further verify the accuracy of the hydrostatic buoyancy force (i.e., Archimede force) computed by Eq. (27), with and without the sub-grid system, two simple benchmark simulations are performed. Case 1 considers a stationary circular cylinder partially submerged in static water, while case 2 involves the same cylinder fully submerged. The theoretical solutions for both cases are known from the Archimede's principle, equal to the weight of the displaced fluid. Under the hydrostatic pressure field, the buoyant force is calculated by the modified GIMEM, and is compared against the results from NS-based IBM developed by Calderer et al. [47] and Borazjani et al. [48]. Despite the simplicity of such a hydrostatic problem, its accuracy is critical for reliably and stably simulating rigid body motion, as it highly relevant to force fluctuation. In both cases, the diameter is D =0.125 m. The simulation domain is $10D \times 11D$ with a water depth of $8D$, where the gravity is 9.81 m/s^2. The relative force error between the evaluated and theoretical values is defined as, Error = $|F_{\mathrm{H}} - F_{\mathrm{H,thero}}|/|F_{\mathrm{H,thero}}|$, where $F_{\mathrm{H,thero}}$ is the theoretical Archimede force. In the present steady-state Archimedes test case, a L2-norm relative residual is defined as,

$$\mathrm{Residual}_{\mathrm{L2}} = \frac{\sqrt{\sum_{\boldsymbol{x}} \left(\varphi^{(n)}(\boldsymbol{x}) - \varphi^{(n-1)}(\boldsymbol{x})\right)^2}}{\sqrt{\sum_{\boldsymbol{x}} \left(\varphi^{(n)}(\boldsymbol{x})\right)^2}} \tag{30}$$

where $\varphi^{(n)}(\boldsymbol{x})$ represents the physical quantities such as density and velocity at the n^{th} time step. The convergence criterion is considered to be satisfied when the maximum residual among all monitored quantities falls below a threshold of 0.001.

Fig. 11 illustrates the vertical velocity field around the stationary cylinder at the 60000$^{\mathrm{th}}$ time step, representing the stable hydrostatic flow field obtained by the developed model. Fig. 12 presents the grid convergence of buoyancy error computed over a series of successively refined uniform meshes with spacing of $\delta x = D/16, D/32, D/64, D/128, D/256$. To evaluate the effectiveness of the sub-grid system, additional tests are conducted on the coarsest mesh $\delta x = D/16$, using the sub-grid spacings defined by $\delta x/(D/16) = 1,\ 3,\ 9,\ 27$. In Fig. 12, the present method achieves a convergence rate better than first order for both cases, with or without the sub-grid system. Although the rate is slightly lower than that reported in [47], the resulting force errors are over one order of magnitude smaller across all grid resolutions. These results confirm that the modified GIMEM can accurately compute the Archimede force and that the integration of a sub-grid system significantly enhances the accuracy of hydrostatic force computations even on coarse meshes.

3.3. Water exit of a circular cylinder

Subsequently, a submerged cylinder rising in still water is used to validate the accuracy and stability of IBB and VOF implementations, in the absence of coupling treatments of them. The cylinder diameter is D =0.125 m. Four cases with different prescribed exit velocities V (V = 0.5124 and 0.7644 m/s), and Reynolds numbers Re (Re =1000 and Re = VD/ν with water viscosity $\nu = 10^{-6}$ m^2/s) are carried out and compared with available data in Ref. [49–51]. Following the numerical simulation by Zhang et al. [49] and Zhu et al. [50], the cylinder is initially at rest at $Vt/D = 3$ and is then accelerated harmonically to a constant velocity at $Vt/D = 2.5$. The simulation domain is $40D \times 11D$ with a water depth of $8D$ and the mesh size is $D/80$. Here, the left and right boundaries are imposed as Neumann outflow condition, and no-slip boundary condition is implemented on the cylinder and bottom boundaries. In the following numerical simulations involving free surface flows, for better numerical stability, the recommended relaxation coefficients in [9] are used, i.e., $\boldsymbol{S} = \mathrm{diag}(1,\ 0.3,\ 1, 1, 1, 1, 1,\ \omega_v,\ \omega_v)$. Fig. 13 illustrates the free surface deformation and vortex distributions when the

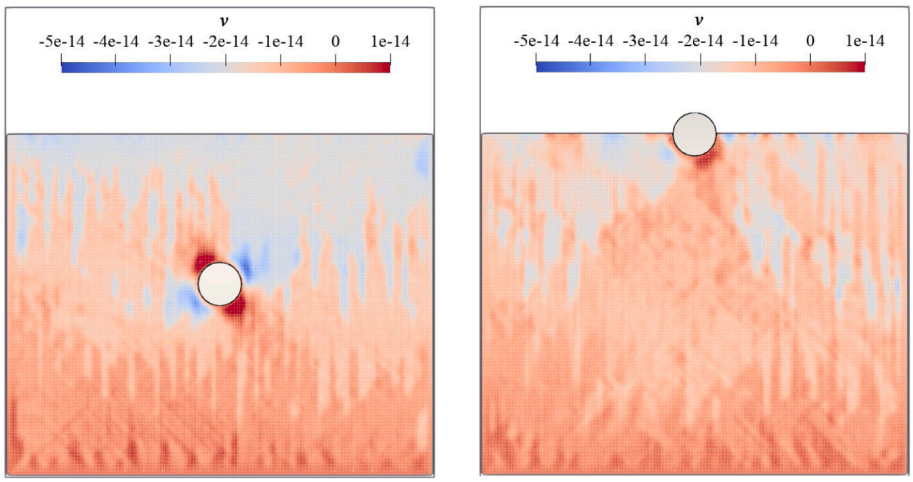

(a) Fully submerged cylinder (b) Partially submerged cylinder

Fig. 11. Vertical velocity field around a stationary cylinder at the 60000$^{\mathrm{th}}$ time step.

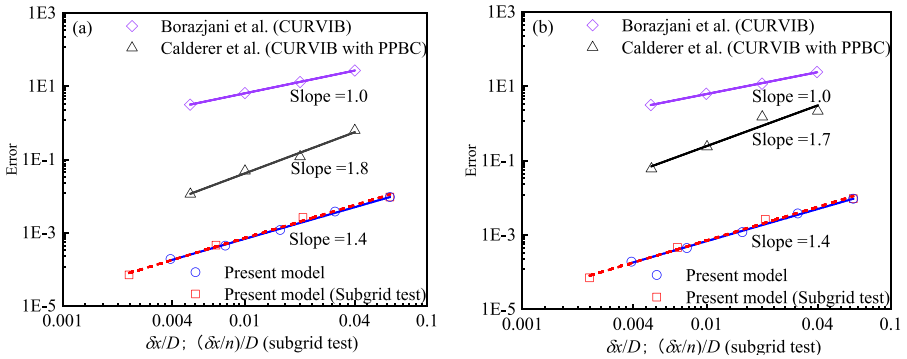

(a) Fully submerged cylinder (b) Partially submerged cylinder

Fig. 12. Grid convergence of the error of hydrostatic buoyancy for a stationary cylinder, compared with IBM of Calderer et al. [47] and Borazjani et al. [48], where CURVIB and PPBC are the curvilinear immersed boundary method and pressure projection boundary condition, respectively.

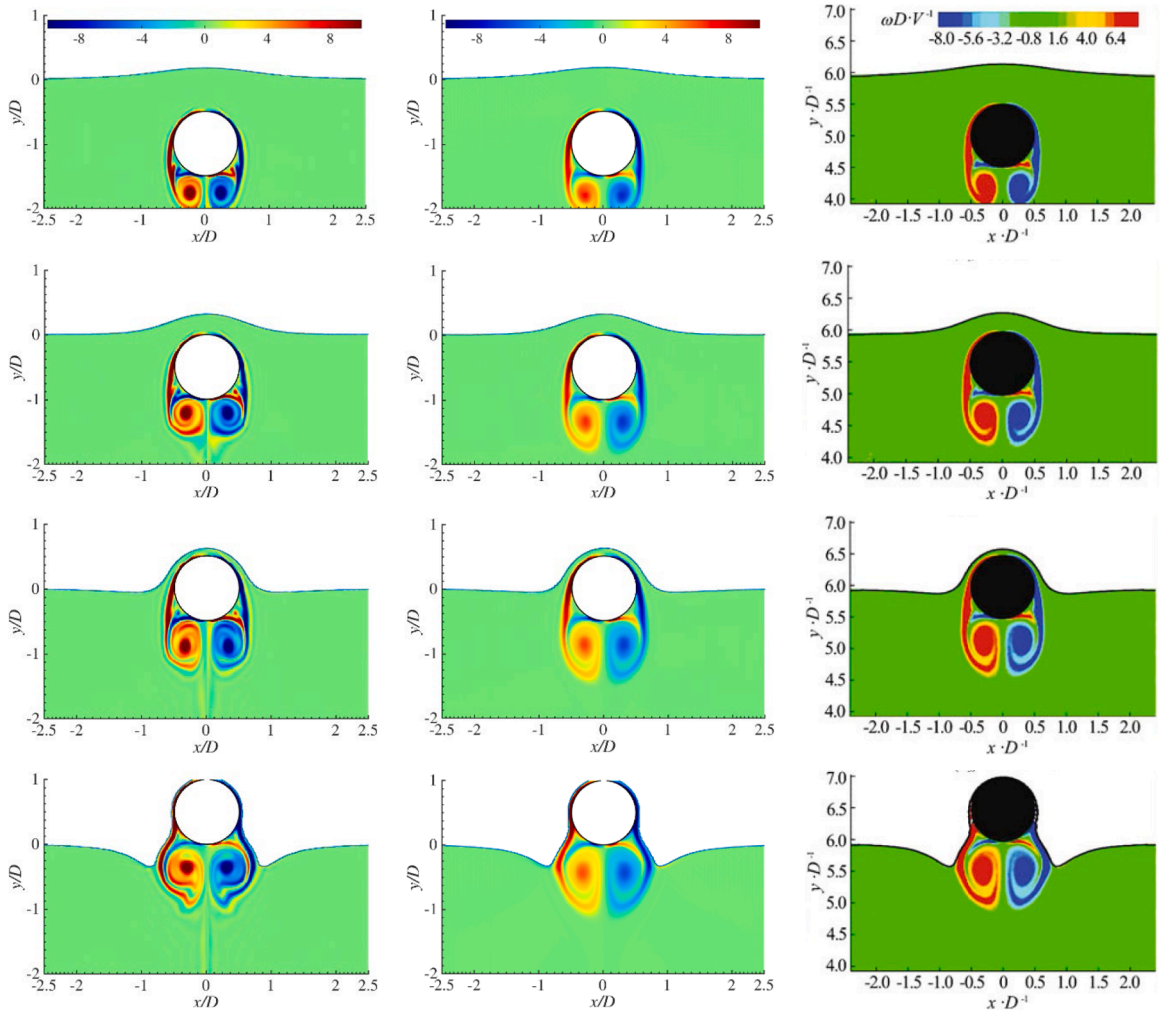

(a) Present model Re $= VD/\nu$ (b) Present model Re =1000 (c) SPH (Re =1000) [49]

Fig. 13. Free surface deformation during water exit of the cylinder with prescribed velocity V =0.7644 m/s, where color denotes the vorticity distribution at four different instants Vt/D = -0.5, 0.0, 0.5 and 1.0.

cylinder velocity is 0.7644 m/s. It can be observed for Re =1000 that the results from the present model are in good agreement with those of Smoothed Particle Hydrodynamics (SPH) model reported in [49]. In both models, the top free surface elevates and both sides cave in, and the wake vortex behind the cylinder gradually stretches and broadens as the cylinder approaches the free surface during cylinder rising. Compared with Re =1000, the case of higher Reynolds number exhibits stronger turbulence and slightly weaker vortex stretching.

The vertical drag force coefficient $C_e = F_y/(0.5\rho V^2 D)$ is illustrated in Figs. 14 and 15. A longer acceleration distance of one Radius is applied to reach specific velocity for stabilizing the drag force in the initial phase. For Re = 1000 in Fig. 14, the present results using mesh sizes $\delta x = D/80$ and $\delta x = D/160$ agree well with that those reported by Zhang et al. [49]. However, the LBM model with lower grid resolution $\delta x = D/40$ shows significant high-frequency force fluctuations. This phenomenon, also observed in studies involving immersed solids interacting with single-phase flows [12,23], is an inherent drawback of numerical simulations with fixed meshes when tracking moving solids. Breugem [52] refers to this issue as "grid locking", which arises because the interpolation operation is not strictly Galilean invariant when a solid object crosses over the grid mesh. Xie et al. [53] discussed this in more detail which is related to the mass conservation of the fresh or dead cut cells. Refining grid can effectively mitigate this issue as $\delta x = D/80$ and $D/160$, though it comes at the cost of increased computational resources for the uniform grid system. Since the mean drag force across the different gird resolutions is approximately identical, a mesh size of $D/80$ is then adopted to reduce computational costs. Fig. 15 illustrates the time histories of C_e for realistic water flows $Re = VD/\nu$ with $\nu = 10^{-6}$ m^2/s, showing good agreement between the LBM model and the experimental results by Miao [51]. The numerical models for both cases ($V = 0.5124$ and 0.7644 m/s) are also in accordance with each other, demonstrating that the proposed GIMEM, with its revised hydrostatic buoyancy formulation, can robustly and stably compute hydrodynamic forces in free surface flows even at high Reynolds numbers, though the flow structures may not be fully resolved at this stage.

3.4. Dam-break flows over an obstacle

The validation continues with a partially submerged stationary structure, where the model's response to violent free surface deformations is assessed. The classical dam-break flow over an obstacle is simulated in this section. This experiment was carried out by Koshizuka [54] and was used by Greaves [55], Issakhov et al. [56] and Meng et al. [57] to validate their NS-based VOF and CLSVOF (coupled level set and volume of fluid) models. Fig. 16 shows the initial conditions and obstacle positions where the initial width (a) of water column equals to 0.146 m. The width and height of this rectangular obstacle are set as 0.024 m and 0.048 m, respectively. The BB scheme is imposed to the slip domain boundaries and non-slip obstacle boundaries. The predicted water surface deformation is compared with experimental results recorded by Koshizuka [54] in Fig. 17, where numerical results obtained with two grid resolutions of $\delta x = a/73$ and $a/146$ are provided. After the dam-break flow encounters the stationary obstacle, the water flow elevates and appears to a highly curved jet flow. It finally collides with the top and left domain boundaries and falls under the gravity. The simulated jet geometry agrees wells with experimental observations, as illustrated in Fig. 17.

3.5. Water entry of a free-falling circular cylinder

In the final two simulations, the entire algorithms involving complex free surface evolution and the motion response of partially submerged floating structures are tested. The water entry of a free-falling circular cylinder has been studied using NS-based model (Larsen [58]), SPH model (Sun et al. [59]), and experiment by Greenhow and Lin [60]. This benchmark case is repeated in this subsection to validate the present gas-liquid-solid model. In the experiment conducted by Greenhow and Lin [60], a cylinder with a diameter D of 0.11 m was initially at rest, dropping freely from a height of 0.5 m above the still water surface. In numerical model, an equivalent case was simulated in [58,59]: the initial velocity was set to 2.938 m/s and the initial bottom of cylinder was just above the free surface. The simulation region is defined as $20D \times 8D$ with water depth of $5D$ and the mesh size of $D/200$. The boundary conditions

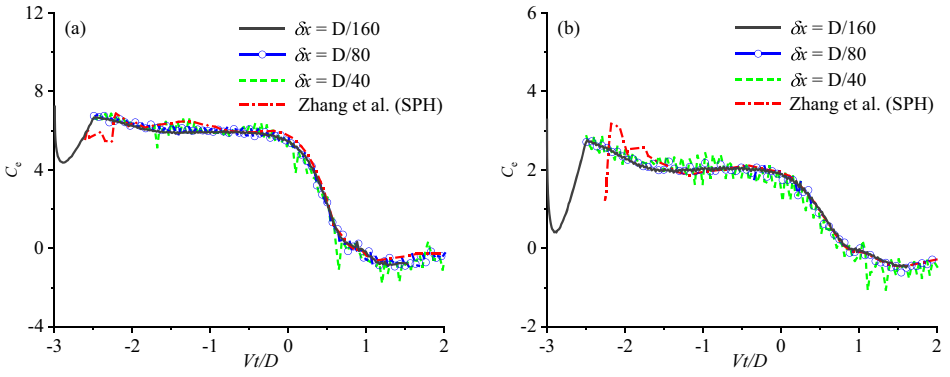

Fig. 14. Comparison of vertical drag force coefficient C_e for Re = 1000, between numerical model by Zhang et al. [49] and the present model. (a) $V = 0.5124$ m/s and (b) $V = 0.7644$ m/s.

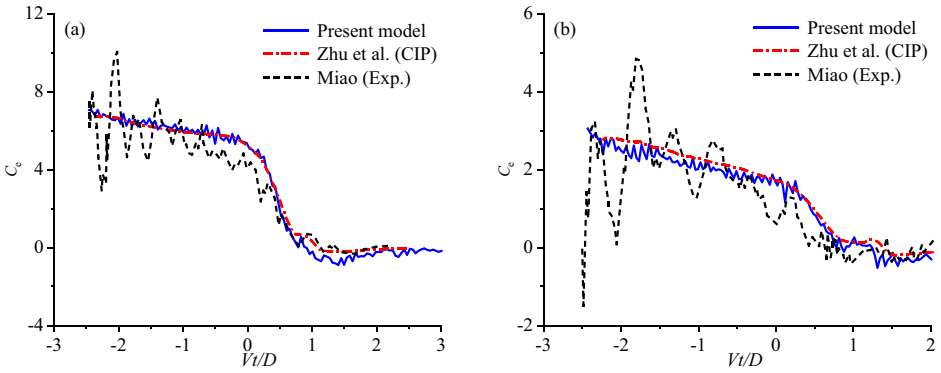

Fig. 15. Comparison of vertical drag force coefficient C_e obtained from the present model with $Re = VD/\nu$ ($\boldsymbol{\nu} = 10^{-6}$ $\boldsymbol{m^2/s}$), numerical model of Zhu et al. [50] and experiment of Miao [51], where CIP is the constrained interpolation profile method. (a) $V = 0.5124$ m/s, and (b) $V = 0.7644$ m/s.

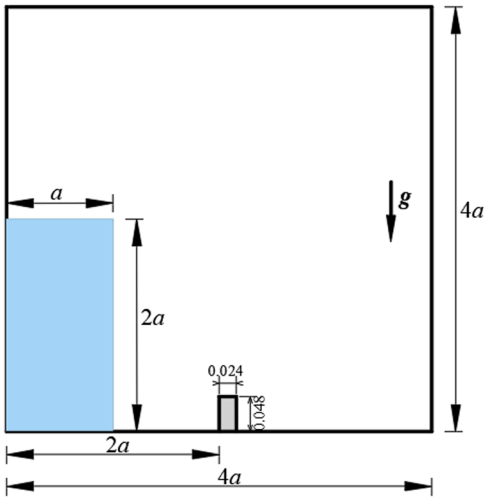

Fig. 16. Initial condition of water column and the obstacle position.

are set the same as that in the water exit case. Since the solid density directly influences the penetration depth, two cases are considered for comparison: one where the solid density equals the water density (i.e., a neutrally buoyant cylinder), and another where it is half that of water (i.e., a half-buoyant cylinder). It is worth noting that the perfectly matched layer technique [61] is applied at the bottom of the simulation tank to absorb the reflected acoustic wave which commonly exists in the compressible fluid solver [59].

We first validate the effectiveness of the proposed model described in Section 2.4. The free surface profiles are compared among the original model, the proposed model with NQIM and the proposed model with both NQIM and BCIM, as shown in Fig. 18. Without the implementation of NQIM and BCIM, the water adheres to the cylinder surface without separation, preventing the formation of the expected jet flow. This unphysical flow pattern leads to the absence of a cavity, resulting in incorrect hydrodynamic forces and penetration depths. Implementing the NQIM can partially correct the jet separation, though some bubbles appear near solid in the absence of BCIM. When both BCIM and NQIM are employed, the jet flow and separation points align well with the experimental snapshots from Greenhow and Lin [60] (see Fig. 19 (c)). Furthermore, Fig. 19 presents the pressure distribution at the initial phase, compared with the numerical results by Sun et al. [59]. It can be observed that the present model yields a symmetrical flow, with pressure decreasing consistently from the symmetric line ($x/D = 2.5$) to far field below the cylinder. Figs. 20 and 21 illustrate the time histories of hydrodynamic force and penetration depth for neutrally buoyant and half-buoyant cases. The neutrally buoyant cylinder, possessing a larger inertia force, penetrates deeper and experiences a greater vertical drag force compared to the half-buoyant cylinder, demonstrating good agreement with the numerical results by Larsen [58]. However, for the half-buoyant case, the numerical simulations predict a deeper penetration compared to the experiment. As noted by Larsen [58], This discrepancy can be attributed to the slightly smaller initial slamming velocity, as the cylinder appears to begin affecting the water surface at $t = 0.285$ s in Greenhow's experiment [60].

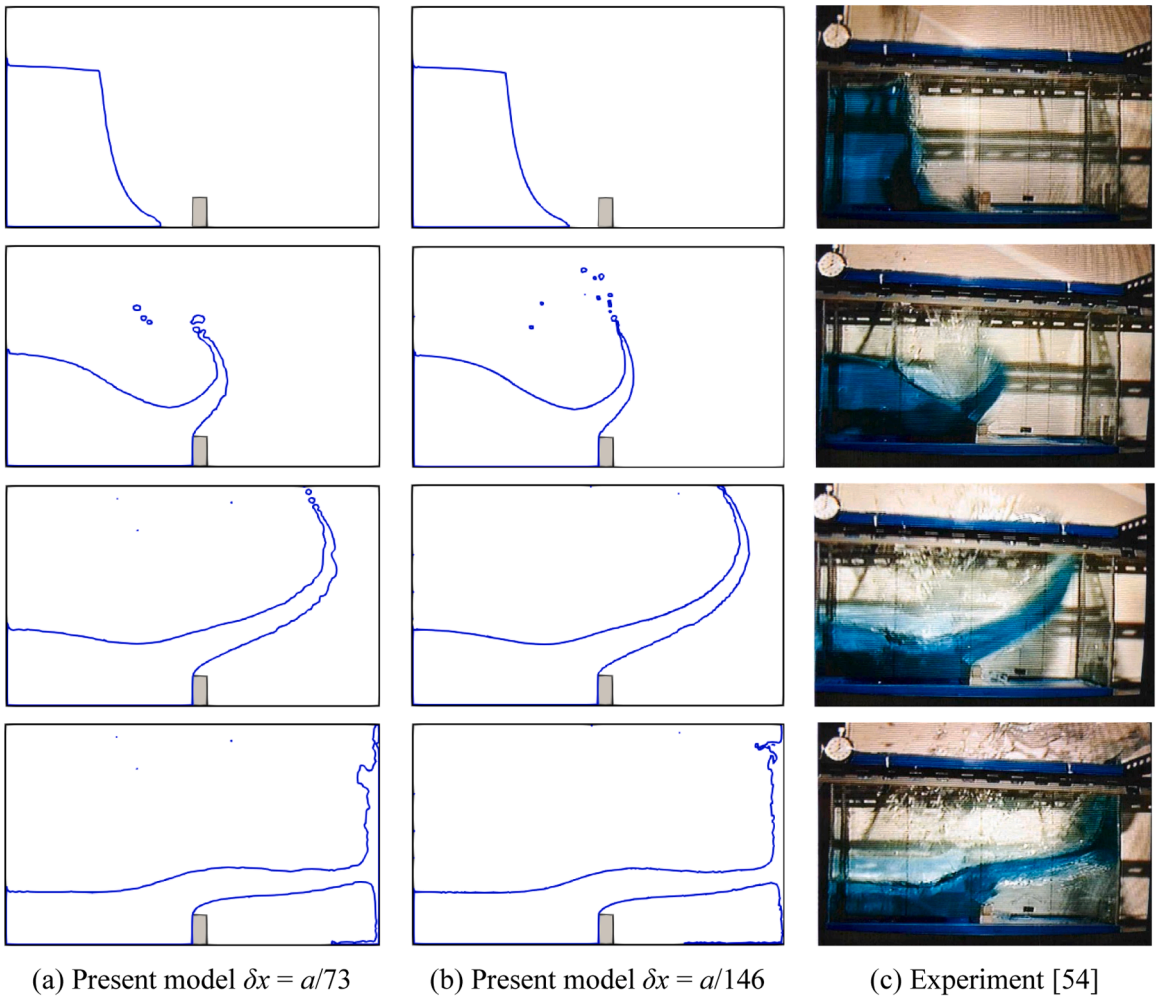

Fig. 17. Comparison of free surface deformation between the present numerical results and experimental observations [54] at different time instants. $t\sqrt{2g/a} = 1.16$, 2.31, 3.47, and 4.63.

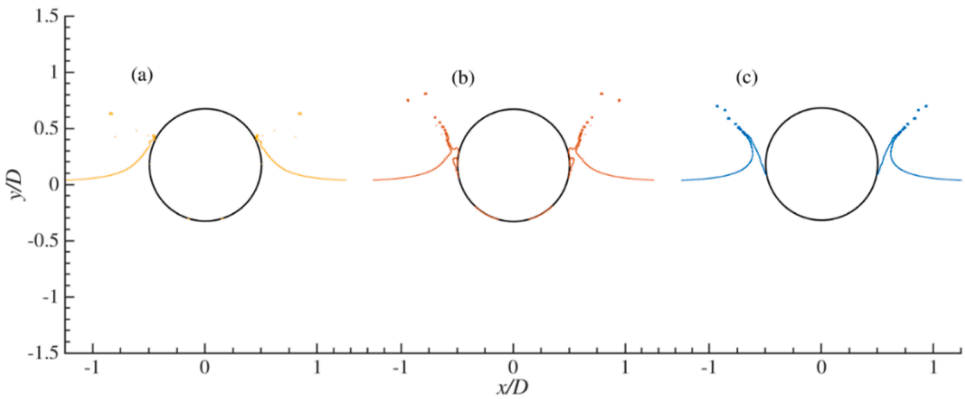

Fig. 18. Free surface deformation at t = 0.015 s for neutral buoyancy. (a) Original algorithm, (b) NQIM without BCIM, (c) NQIM and BCIM.

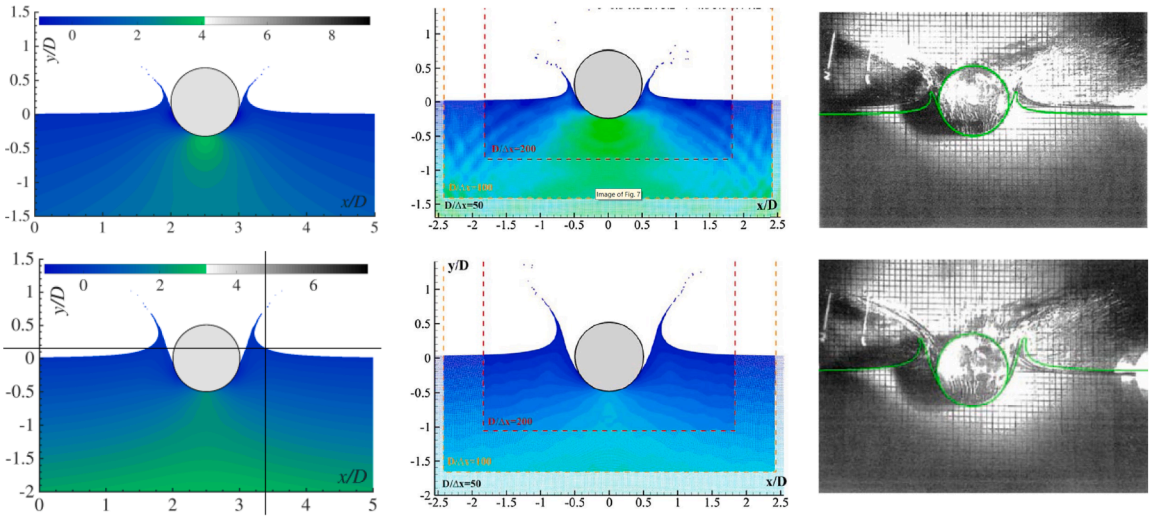

Fig. 19. Free surface deformation during the initial instant of a cylinder's water entry, where the color represents the pressure. The first row: neutrally buoyant cylinder at $t = 0.015$ s. The second row: half-buoyant cylinder at $t = 0.03$ s. The green line in experiment results denotes numerical solutions from a boundary element method in [62].

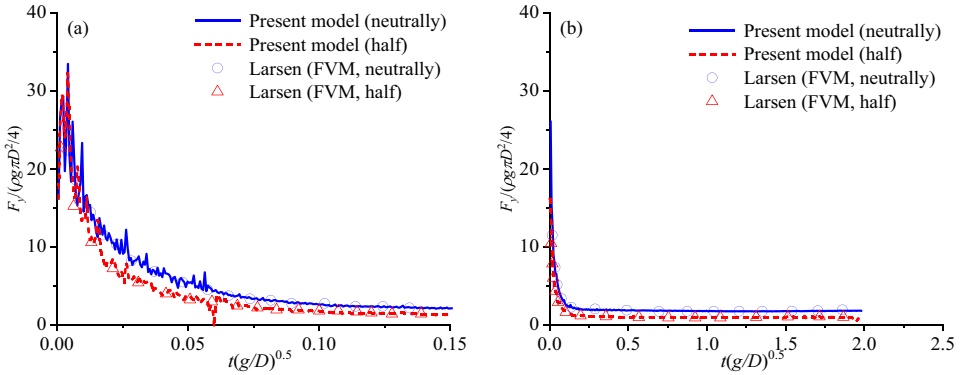

Fig. 20. Total vertical force versus t during the water entry of the cylinder compared with numerical results by Larsen [58].(a) The initial phase and (b) overview.

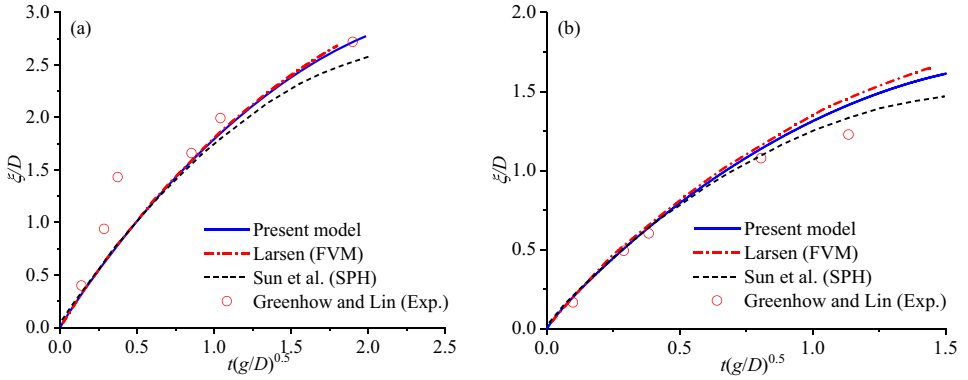

Fig. 21. Penetration depth ξ versus t during the water entry of the cylinder compared with published results in Larsen [58], Sun et al. [59], and Greenhow and Lin [60]. (a) Neutrally buoyant cylinder and (b) half-buoyant cylinder.

3.6. Free-floating box interacted with water waves

To validate the complete gas-liquid-solid model under dynamic conditions, the sway, heave, and roll motions of a rectangular floater under nonlinear waves are numerically investigated, and compared with experimental and numerical results by Ren et al. [63,64]. As illustrated in Fig. 22, a classic momentum source method is implemented in the wave generation domain and the sponge layer to generate and dissipate the incident waves, respectively. In this approach, the equivalent generating $\boldsymbol{S}_g$ and damping $\boldsymbol{S}_d$ forces as expressed in Eq. (31) are incorporated into the lattice Boltzmann equation [28,65]. The half-buoyant box-shaped structure has a draft of 0.1 m, density of 500 kg/m^3 and width of 0.3 m. Table 1 summarizes all parameters of the box and the numerical wave tank (NWT), and the mesh size is set as $\delta x = d/200$. The Neumann outflow condition is implemented at left and right boundaries and no-slip condition is imposed at the box and tank bottom.

$$\begin{cases} S_{g,x} = g(2\beta(x - x_s))e^{-\beta(x-x_s)^2}\dfrac{\delta}{A\omega}(A_1\cos\theta + A_2\cos 2\theta) \\ S_{g,y} = 0 \end{cases} \tag{31}$$

$$\boldsymbol{S}_d = -B_1 u \frac{e^{\left|\frac{x-x_0}{L_s}\right|^{n_s}} - 1}{e - 1}$$

where $\beta = 20/W^2$ is a coefficient of source width W; x_s is the centre of wave generating area. The distribution source density δ and angle θ can be expressed as,

$$\delta = \frac{2A\left(\omega^2 - \alpha_1 g k^4 d^3\right)}{\omega I k\left(1 - \alpha(kd)^2\right)} \tag{32}$$

$$\theta = \frac{\pi}{2} - \omega t - \arcsin\left[\left(-A_1 + \sqrt{A_1^2 + 8A_2^2}\right) \Big/ (4A_2)\right] \tag{33}$$

where A is the first-order wave amplitude; $A_1 = A$ and $A_2 = \frac{A^2 k \cosh kd}{4\sinh^3 kd}$; $\alpha = -0.38955$ and $\alpha_1 = \alpha + 1/3$ is a coefficient of the basic Boussinesq equation; d is the still water depth; $k = 2\pi/L$ is the wavenumber and L is the wavelength; $I = \sqrt{\pi/\beta}e^{-k^2/4\beta}$.

For the damping force $\boldsymbol{S}_d$, B_1 and n_s are empirical coefficients; x_0 and L_s are the starting location and width of the sponge layer, respectively. The corresponding details can be found in [28,65].

In the absence of wave generation, a rolling oscillation of this floating box damped by water viscosity is first simulated to validate rotation mode as a supplement to the translation mode discussed in Section 3.5. The box is homogeneous, with its center fixed at the initial position, and the initial angle of inclination set to 0.209 radians (12°). The time history of the rolling angle, simulated using the developed LBM model, is compared with the numerical and experimental result by Ren et al. [63,64] in Fig. 23. It can be observed the present LBM model accurately predicts both the damped response amplitude and the natural rolling period.

All simulations based on LBM are performed on the UK National High-Performance Computing service, Archer2. Each node of Archer2 is equipped with dual AMD EPYC™ 7742 64-core CPUs. For the 2D wave-box interaction, a simulation consisting of 3.5 million grid cells and 0.7 million time steps, costs approximately 4 hours using 4 nodes. Table 2 lists the wall time and mesh configuration of two representative cases, incorporating the complete gas-liquid-solid coupling under wave dynamics conditions. These cases correspond to the weakest and strongest nonlinear wave conditions in the free-floating box interacting with Stokes waves.

Due to the mean horizontal drift force, a floating structure subjected to Stokes waves will move forward in the direction of wave propagation [63,64]. This wave-structure interaction case serves to validate results for the floating structure interactions with free surface flows. Here, x_c, y_c and θ_c are represented as the horizontal displacement and vertical displacement and rolling angle of this floating box, respectively. Fig. 24 presents horizontal motion x_c of the free-floating box under regular waves with a wave period of T=

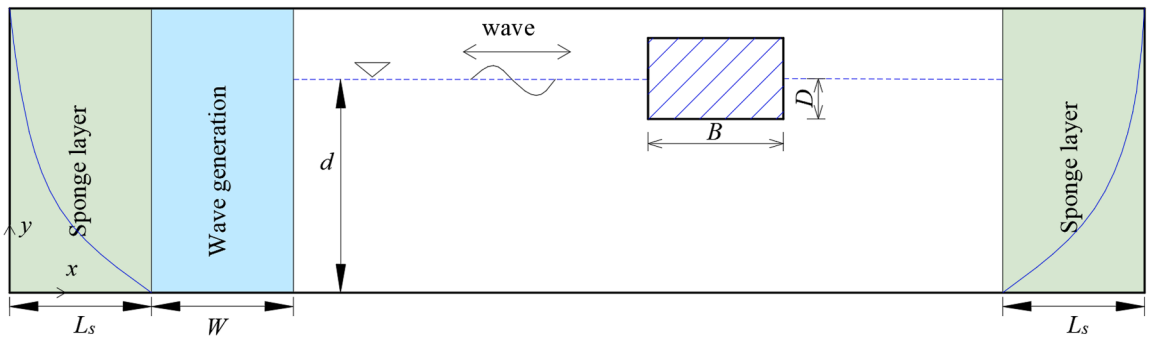

Fig. 22. Sketch of the NWT and a rectangular box placed inside.

Table 1
Parameters for the free-floating box interacting with waves.

NWT	Length (m)	Height (m)	d (m)	Box	D (m)	B (m)	H_b (m)
	$10L$	$1.5d$	0.4		0.1	0.3	0.2
Wave Absorption	B_1 (s^{-1})	n_s	L_s (m)	Wave Generation	W (m)		
	20	2	$2L$		L		

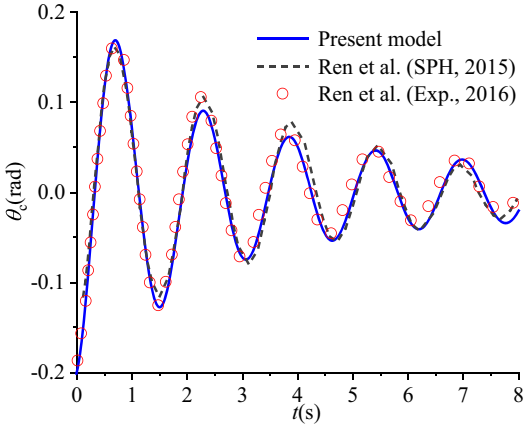

Fig. 23. Time histories of the roll angle during damped rolling oscillation of the floating box, obtaining from the present model, the SPH model and experiment by Ren et al. [63,64].

Table 2
Wall time and mesh sizes for two representative wave conditions (low and high nonlinearity) in free-floating box simulations with Stokes waves.

Wave height H (m)	Lattice cells	Wall time T_W (hr)
0.04	10000 × 350	3.89
0.10	10000 × 350	4.12

1.2 s and wave heights of H= 0.04, 0.06, 0.08, 0.1 m, In Fig. 24, the floating box drifts in the direction of wave propagation accompanied by a periodic sway motion. Also, the drift speed increases with the increase of wave height as the mean drift force increases with wave steepness. Fig. 25 further illustrates the heave motion and roll motions under the highest wave with the strongest wave nonlinearity, $H = 0.1$ m. It can be observed that the oscillation period of the floating box is slightly longer than wave period of the incident wave. It is induced by the drift motion. To be specific, as the floating body drifts forward after one wave period, the next train of incident waves requires additional time to catch up and reach the floating body. Fig. 26 illustrates the motion attitude of this floating box and the wave surface elevation during a motion cycle. At the initial time $t = 0$, the wave crest approaches the floating box with a rolling angle of zero. The box first rotates clockwise and drifts rightwards from 0 to $T/4$, then rotates anticlockwise while continuing to drift forwards from $T/4$ to $T/2$. Following the wave trough, the box drifts leftwards from $T/2$ to $3T/4$, and finally rotates clockwise from $3T/4$ to $1.1T$ to return to the initial state at $1.1T$. Compared to the motion trajectory and free surface elevation with experimental and numerical results, the present LBM model can well predict the oscillation period, oscillation amplitude, and drift motion of the floating box under nonlinear waves. In conclusion, this model validation demonstrates that the present model is capable of accurately and stably simulating floating rigid bodies interaction with water waves.

4. Conclusions

In this study, the volume-of-fluid method (VOF) and interpolated bounce back- Galilean-Invariant momentum exchange method (IBB-GIMEM), are incorporated into lattice Boltzmann method (MRT-LBM) in the dynamic pressure framework, for investigating floating rigid bodies interacting with free surface flows. For extension to partially submerged bodies, the GIMEM in the IBB-based FSI approaches is revised to take the absolute atmospheric pressure and hydrostatic pressure gradient into account. For accurately identifying gas-liquid-solid interface near a floating structure, we present and couple phase state conversion rules for gas-liquid and liquid-solid interfaces in VOF and FSI approaches, and appropriately address the boundary conditions of a triple junction cell which is occupied by three phases - gas, liquid, and solid, according to geometric parameters, i.e., the free surface normal vectors. The IBB-LBM solver has been validated through six classical fluid-structure interaction cases, covering scenarios from immersed to floating structures, and from single-phase flows to free surface flows including water waves.

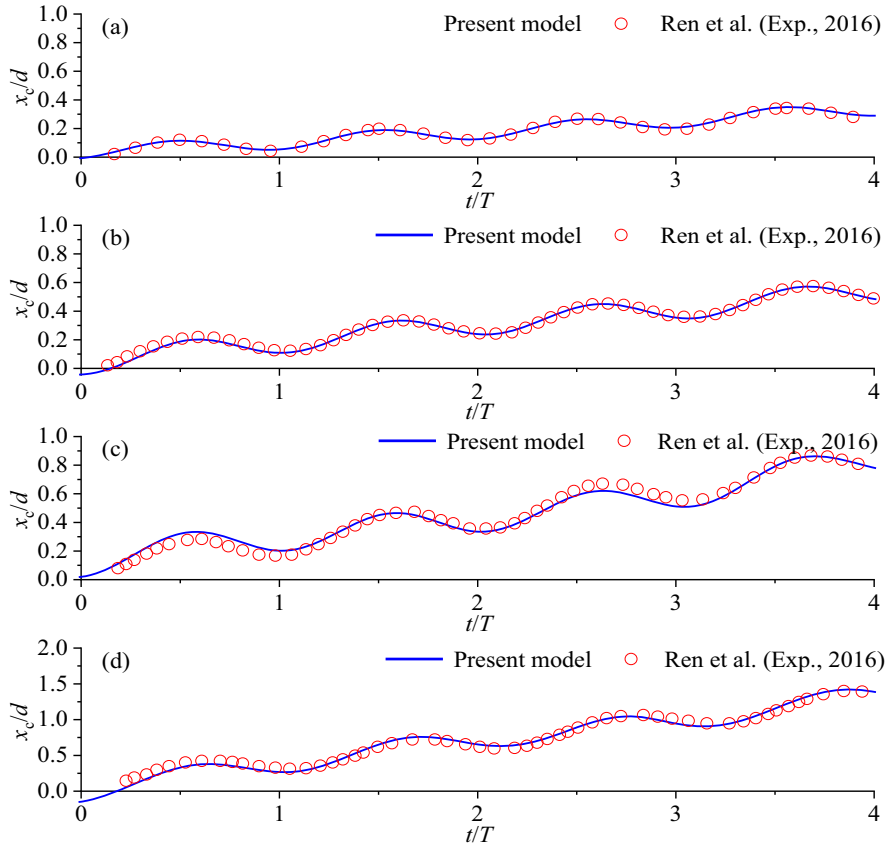

Fig. 24. Time histories of the sway motion of the floating box for different wave heights, obtained from the present model and the experiment [63]. (a) H =0.04 m, (b) H =0.06 m, (c) H =0.08 m and (d) H =0.1 m, with T =1.2 s.

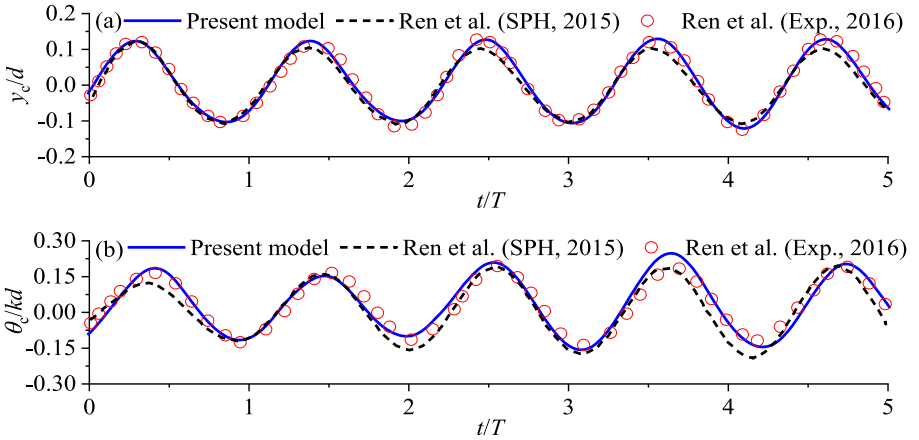

Fig. 25. Time histories of the heave and roll motions of the floating box under the wave condition of H =0.1 m and T =1.2 s, obtained from the present model and the experiment [63].

First, the free settling of an immersed circular solid in single-phase flows was simulated to verify the code implementation and the revised GIMEM, together with Archimede force test cases. Next, a rising cylinder with a prescribed constant velocity in free surface flow was simulated, involving the indirect interaction between IBB-based FSI and VOF approaches. The consistent wake vortex and free surface elevation with those published results presented the reliability of this model on simulating immersed structure in free surface flows. Following the immersed bodies, studies on partially submerged structures coupling with free surface flows were then conducted, ranging from stationary to moving ones, including dam-break flows over obstacles, a freely falling cylinder, and wave

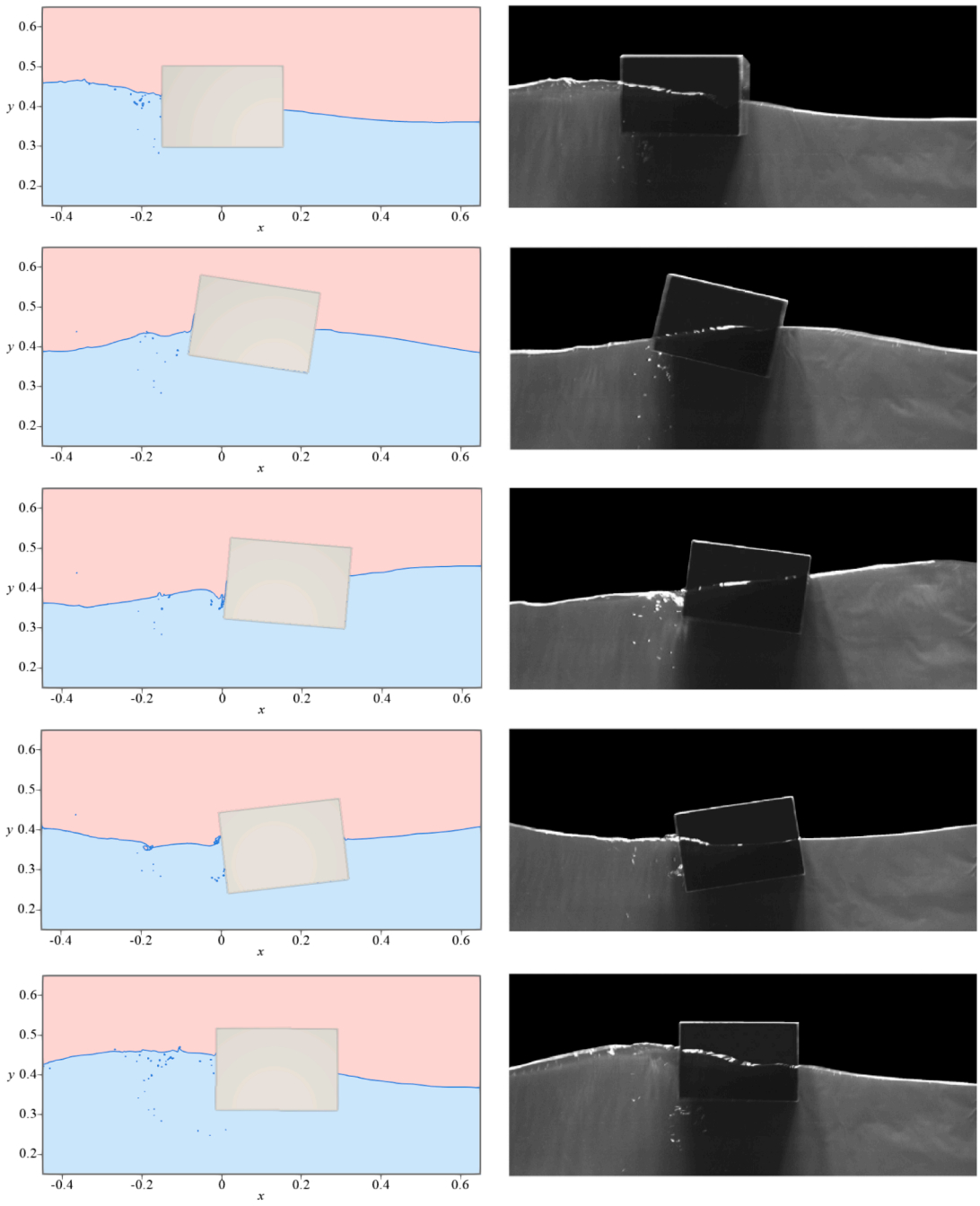

Fig. 26. Comparison of floating box locations and wave surface elevation between the present LBM, and experiment [63] at five instants, t=0, 0.25T, 0.50T, 0.75T, and 1.10T for H =0.1 m and T =1.2 s.

interaction with a floating box. The violent free surface deformation observed in dam-break flows demonstrated stability and accuracy of the current LBM model for free surface simulations and their interaction with fixed structures. Partially submerged moving structures require coupling treatment of VOF and IBB-based FSI approaches. To validate the proposed gas-liquid-solid treatments, the free-falling cylinder of which the motion is determined by the hydrodynamic force and gravity, was simulated. The resulting jet flow, liquid separation points at cylinder, and penetration depth are aligned well with the experimental data, demonstrating the effectiveness of this model in addressing unphysical free surface deformation, with the revised GIMEM proving effective for floating bodies. Moreover, wave interaction with a free-floating box was investigated for validating the capability in complex dynamic conditions and

motion responses.

Overall, a two-dimensional free surface FSI-LBM model has been proposed for investigating floating bodies interacting with free surface flows. Due to LBM's inherently modular and localized computational framework, it offers a flexible basis for extending the developed model to engineering applications, such as renewable energy systems (e.g., offshore wind turbines and wave energy farms) and marine aquaculture systems. Further efforts will be focused on two aspects: (1) extending the current model into a three-dimensional framework and also by integrating it with a pneumatic model to study wave interactions with an elastically constrained floating oscillating water column wave energy converter; (2) further reducing the force fluctuation issue caused by the mass conservation error of the fresh or dead cut cells.

CRediT authorship contribution statement

Baoming Guo: Writing – original draft, Visualization, Validation, Software, Methodology. **Jianping Meng:** Writing – review & editing, Supervision, Software, Methodology, Funding acquisition. **Dezhi Ning:** Writing – review & editing, Supervision. **Zhihua Xie:** Writing – review & editing, Supervision, Methodology, Funding acquisition. **Shunqi Pan:** Writing – review & editing, Supervision, Methodology, Funding acquisition.

Declaration of competing interest

The authors declare that they have no known competing financial interests or personal relationships that could have appeared to influence the work reported in this paper.

Acknowledgements

Support from the UK Engineering and Physical Sciences Research Council under the projects "UK Consortium on Mesoscale Engineering Sciences (UKCOMES)" (Grant No. EP/X035875/1) and wave energy converter project (Grant No. EP/V040235/1) is gratefully acknowledged. This work made use of computational support by CoSeC, the Computational Science Centre for Research Communities, through UKCOMES. This work has also been supported by Cardiff University Scholarship and China Scholarship Council (202006060048).

Data availability

Data will be made available on request.

References

[1] F. Dias, J.-M. Ghidaglia, Slamming: recent progress in the evaluation of impact pressures, Annu. Rev. Fluid Mech. 50 (2018) 243–273.
[2] R. Wang, D. Ning, C. Zhang, Q. Zou, Z. Liu, Nonlinear and viscous effects on the hydrodynamic performance of a fixed OWC wave energy converter, Coast. Eng. 131 (2018) 42–50.
[3] R. Mayon, D. Ning, Y. Sun, Z. Ding, R. Wang, Y. Zhou, Experimental investigation on a novel and hyper-efficient oscillating water column wave energy converter coupled with a parabolic breakwater, Coast. Eng. (2023) 185.
[4] R. Zhang, Y. Chen, J. Lei, X. Zhou, P. Yao, M.J.F. Stive, Experimental investigation of wave attenuation by mangrove forests with submerged canopies, Coast. Eng. 186 (2023).
[5] X. Shan, X.-F. Yuan, H. Chen, Kinetic theory representation of hydrodynamics: a way beyond the Navier–Stokes equation, J. Fluid Mech. (2006) 550.
[6] J.H. Ferziger. Computational Methods for Fluid Dynamics, 2002.
[7] T. Krüger, H. Kusumaatmaja, A. Kuzmin, O. Shardt, G. Silva, E.M. Viggen, The Lattice Boltzmann Method, Springer, Cham, 2017.
[8] Y. Sun, C.H. Rycroft, A fully-integrated lattice Boltzmann method for fluid–structure interaction, J. Comput. Phys. 526 (2025).
[9] G. Liu, J. Zhang, Q. Zhang, A high-performance three-dimensional lattice Boltzmann solver for water waves with free surface capturing, Coast. Eng. (2021) 165.
[10] C. Schwarzmeier, M. Holzer, T. Mitchell, M. Lehmann, F. Häusl, U. Rüde, Comparison of free-surface and conservative Allen-Cahn phase-field lattice Boltzmann method, J. Comput. Phys. (2023) 473.
[11] H.E. Morrison, A. Leder, Sediment transport in turbulent flows with the lattice Boltzmann method, Comput. Fluids 172 (2018) 340–351.
[12] C. Peng, Y. Teng, B. Hwang, Z. Guo, L.-P. Wang, Implementation issues and benchmarking of lattice Boltzmann method for moving rigid particle simulations in a viscous flow, Comput. Math. Appl. 72 (2016) 349–374.
[13] C. Peng, O.M. Ayala, L.-P. Wang, A comparative study of immersed boundary method and interpolated bounce-back scheme for no-slip boundary treatment in the lattice Boltzmann method: part I, laminar flows, Comput. Fluids 192 (2019).
[14] A.J.C. Ladd, Numerical simulations of particulate suspensions via a discretized Boltzmann equation. Part 1. Theoretical foundation, J. Fluid Mech. 271 (2006) 285–309.
[15] Z. Xie, T. Stoesser, A three-dimensional Cartesian cut-cell/volume-of-fluid method for two-phase flows with moving bodies, J. Comput. Phys. 416 (2020) 109536.
[16] R. Mei, W. Shyy, D. Yu, L.S. Luo, Lattice Boltzmann method for 3-D flows with curved boundary, J. Comput. Phys. 161 (2000) 680–699.
[17] D.Z. Yu, R.W. Mei, L.S. Luo, W. Shyy, Viscous flow computations with the method of lattice Boltzmann equation, Prog. Aerosp. Sci. 39 (2003) 329–367.
[18] L. Chen, Y. Yu, J. Lu, G. Hou, A comparative study of lattice Boltzmann methods using bounce-back schemes and immersed boundary ones for flow acoustic problems, Int. J. Numer. Methods Fluids 74 (2014) 439–467.
[19] C.S. Peskin, Numerical analysis of blood flow in the heart, J. Comput. Phys. 25 (1977) 220–252.
[20] H. Li, X. Lu, H. Fang, Y. Qian, Force evaluations in lattice Boltzmann simulations with moving boundaries in two dimensions, Phys. Rev. E. Stat. Nonlin. Soft. Matter. Phys. 70 (2004) 026701.
[21] R. Mei, D. Yu, W. Shyy, L.S. Luo, Force evaluation in the lattice Boltzmann method involving curved geometry, Phys. Rev. E. Stat. Nonlin. Soft. Matter. Phys. 65 (2002) 041203.
[22] Y. Chen, Q. Cai, Z. Xia, M. Wang, S. Chen, Momentum-exchange method in lattice Boltzmann simulations of particle-fluid interactions, Phys. Rev. E. Stat. Nonlin. Soft. Matter. Phys. 88 (2013) 013303.

[23] B. Wen, C. Zhang, Y. Tu, C. Wang, H. Fang, Galilean invariant fluid–solid interfacial dynamics in lattice Boltzmann simulations, J. Comput. Phys. 266 (2014) 161–170.
[24] Z. Li, G. Oger, D.Le Touzé, A partitioned framework for coupling LBM and FEM through an implicit IBM allowing non-conforming time-steps: application to fluid-structure interaction in biomechanics, J. Comput. Phys. (2022) 449.
[25] J.C.B. de Motta, P. Costa, J.J. Derksen, C. Peng, L.P. Wang, W.P. Breugem, et al., Assessment of numerical methods for fully resolved simulations of particle-laden turbulent flows, Comput. Fluids 179 (2019) 1–14.
[26] C. Peng, O.M. Ayala, J.C.B. de Motta, L.P. Wang, A comparative study of immersed boundary method and interpolated bounce-back scheme for no-slip boundary treatment in the lattice Boltzmann method: part II, turbulent flows, Comput. Fluids 192 (2019).
[27] C. Korner, M. Thies, T. Hofmann, N. Thurey, U. Rude, Lattice Boltzmann model for free surface flow for modeling foaming, J. Stat. Phys. 121 (2005) 179–196.
[28] G. Liu, Q. Zhang, J. Zhang, Numerical wave simulation using a modified lattice Boltzmann scheme, Comput. Fluids 184 (2019) 153–164.
[29] K. Sato, K. Kawasaki, S. Koshimura, A comparative study of the cumulant lattice Boltzmann method in a single-phase free-surface model of violent flows, Comput. Fluids (2022) 236.
[30] C. Janssen, M. Krafczyk, A lattice Boltzmann approach for free-surface-flow simulations on non-uniform block-structured grids, Comput. Math. Appl. 59 (2010) 2215–2235.
[31] C. Janßen, M. Krafczyk, Free surface flow simulations on GPGPUs using the LBM, Comput. Math. Appl. 61 (2011) 3549–3563.
[32] Y. Thorimbert, J. Latt, L. Cappietti, B. Chopard, Virtual wave flume and oscillating Water Column modeled by lattice Boltzmann method and comparison with experimental data, Int. J. Mar. Energy 14 (2016) 41–51.
[33] C.F. Janssen, S.T. Grilli, M. Krafczyk, On enhanced non-linear free surface flow simulations with a hybrid LBM-VOF model, Comput. Math. Appl. 65 (2013) 211–229.
[34] A. Badarch, J.D. Fenton, T. Hosoyamada, Application of free-surface immersed-boundary lattice Boltzmann method to waves acting on coastal structures, J. Hydraul. Eng. (2020) 146.
[35] D.R. Noble, J.R. Torczynski, A Lattice-Boltzmann method for partially saturated computational cells, Int. J. Mod. Phys. C 09 (2011) 1189–1201.
[36] Y. Xiao, G. Zhang, D. Hui, H. Yan, S. Feng, S. Wang, Numerical simulation for water entry and exit of rigid bodies based on the immersed boundary-lattice Boltzmann method, J. Fluids Struct. 109 (2022).
[37] H.H. Hao, Y.P. Song, J.Y. Yu, F. Chen, T. Liu, Numerical analysis of water exit for a sphere with constant velocity using the lattice Boltzmann method, Appl. Ocean Res. 84 (2019) 163–178.
[38] Z. Liu, X. Feng, W. Li, F. Tian. An immersed boundary-Lattice Boltzmann method based on the adaptive mesh refinement for free surface flows in ocean engineering applications. Available at SSRN: https://ssrn.com/abstract=4353540 or 10.2139/ssrn.4353540.
[39] S. Bogner, U. Rüde, Simulation of floating bodies with the lattice Boltzmann method, Comput. Math. Appl. 65 (2013) 901–913.
[40] S. Majumder, A. Ghosh, D.N. Basu, G. Natarajan, Re-examining the partially saturated-cells method for incompressible flows with stationary and moving bodies, Comput. Math. Appl. 110 (2022) 19–39.
[41] P.L. Bhatnagar, E.P. Gross, M. Krook, A model for collision processes in gases. I. Small amplitude processes in charged and neutral one-component systems, Phys. Rev. 94 (1954) 511–525.
[42] Z.L. Guo, C.G. Zheng, B.C. Shi, Discrete lattice effects on the forcing term in the lattice Boltzmann method, Phys. Rev. E (2002) 65.
[43] P. Lallemand, L.S. Luo, Theory of the lattice Boltzmann method: dispersion, dissipation, isotropy, Galilean invariance, and stability, Phys. Rev. E 61 (2000) 6546–6562.
[44] J. Meng, Y. Zhang, N.G. Hadjiconstantinou, G.A. Radtke, X. Shan, Lattice ellipsoidal statistical BGK model for thermal non-equilibrium flows, J. Fluid Mech. 718 (2013) 347–370.
[45] M. Krafczyk, J. Tölke, L.-S. Luo, Large-eddy simulations with a multiple-relaxation-time LBE model, Int. J. Mod. Phys. B 17 (2003) 33–39.
[46] R. Mei, L.-S. Luo, P. Lallemand, D. d'Humières, Consistent initial conditions for lattice Boltzmann simulations, Comput. Fluids 35 (2006) 855–862.
[47] A. Calderer, S. Kang, F. Sotiropoulos, Level set immersed boundary method for coupled simulation of air/water interaction with complex floating structures, J. Comput. Phys. 277 (2014) 201–227.
[48] I. Borazjani, L. Ge, F. Sotiropoulos, Curvilinear immersed boundary method for simulating fluid structure interaction with complex 3D rigid bodies, J. Comput. Phys. 227 (2008) 7587–7620.
[49] A.M. Zhang, P.N. Sun, F.R. Ming, A. Colagrossi, Smoothed particle hydrodynamics and its applications in fluid-structure interactions, J. Hydrodyn. 29 (2017) 187–216.
[50] X. Zhu, O.M. Faltinsen, C. Hu, Water entry and exit of a horizontal circular cylinder, in: 24th International Conference on Offshore Mechanics and Arctic Engineering: Volume 1, Parts A and B, 2005, pp. 647–658.
[51] G. Miao. Hydrodynamic forces and dynamic responses of circular cylinders in wave zones 1989.
[52] W.P. Breugem, A second-order accurate immersed boundary method for fully resolved simulations of particle-laden flows, J. Comput. Phys. 231 (2012) 4469–4498.
[53] Z. Xie, P. Lin, T. Stoesser, A conservative and consistent implicit Cartesian cut-cell method for moving geometries with reduced spurious pressure oscillations, J. Comput. Phys. 459 (2022) 111124.
[54] S. Koshizuka, A particle method for incompressible viscous flow with fluid fragmentation, Comp Fluid Dyn 4 (1995) 29–46.
[55] D.M. Greaves, Simulation of viscous water column collapse using adapting hierarchical grids, Int. J. Numer. Methods Fluids 50 (2006) 693–711.
[56] A. Issakhov, Y. Zhandaulet, A. Nogaeva, Numerical simulation of dam break flow for various forms of the obstacle by VOF method, Int. J. Multiph. Flow 109 (2018) 191–206.
[57] W.K. Meng, C.H. Yu, J. Li, R.D. An, Three-dimensional simulation of silted-up dam-break flow striking a rigid structure, Ocean Eng. (2022) 261.
[58] E. Larsen, Impact Loads on Circular Cylinders, Norwegian University of Science and Technology, 2013.
[59] P. Sun, A.M. Zhang, S. Marrone, F. Ming, An accurate and efficient SPH modeling of the water entry of circular cylinders, Appl. Ocean Res. 72 (2018) 60–75.
[60] M. Greenhow, W. M. Lin. Nonlinear free-surface effects: experiments and theory. 1983.
[61] A. Najafi-Yazdi, L. Mongeau, An absorbing boundary condition for the Lattice Boltzmann method based on the perfectly matched layer, Comput. Fluids 68 (2012) 203–218.
[62] H. Sun, O.M. Faltinsen, Water impact of horizontal circular cylinders and cylindrical shells, Appl. Ocean Res. 28 (2006) 299–311.
[63] M. He, B. Ren, D.H. Qiu, Experimental study of nonlinear behaviors of a free-floating body in waves, China Ocean Eng. 30 (2016) 421–430.
[64] B. Ren, M. He, P. Dong, H. Wen, Nonlinear simulations of wave-induced motions of a freely floating body using WCSPH method, Appl. Ocean Res. 50 (2015) 1–12.
[65] J. Choi, S.B. Yoon, Numerical simulations using momentum source wave-maker applied to RANS equation model, Coast. Eng. 56 (2009) 1043–1060.